

Charge Transport in and Electroluminescence from sp³-Functionalized Carbon Nanotube Networks

Nicolas F. Zorn¹, Felix J. Berger¹, and Jana Zaumseil^{1}*

¹ Institute for Physical Chemistry and Centre for Advanced Materials, Universität Heidelberg,

D-69120 Heidelberg, Germany

Corresponding Author

*E-mail: zaumseil@uni-heidelberg.de

ABSTRACT

The controlled covalent functionalization of semiconducting single-walled carbon nanotubes (SWCNTs) with luminescent sp^3 defects leads to additional narrow and tunable photoluminescence features in the near-infrared and even enables single-photon emission at room temperature, thus strongly expanding their application potential. However, the successful integration of sp^3 -functionalized SWCNTs in optoelectronic devices with efficient defect state electroluminescence not only requires control over their emission properties but also a detailed understanding of the impact of functionalization on their electrical performance, especially in dense networks. Here, we demonstrate ambipolar, light-emitting field-effect transistors based on networks of pristine and functionalized polymer-sorted (6,5) SWCNTs. We investigate the influence of sp^3 defects on charge transport by employing electroluminescence and (charge-modulated) photoluminescence spectroscopy combined with temperature-dependent current-voltage measurements. We find that sp^3 -functionalized SWCNTs actively participate in charge transport within the network as mobile carriers efficiently sample the sp^3 defects, which act as shallow trap states. While both hole and electron mobilities decrease with increasing degree of functionalization, the transistors remain fully operational, showing electroluminescence from the defect states that can be tuned by the defect density.

KEYWORDS

single-walled carbon nanotubes, covalent functionalization, sp^3 defects, electroluminescence, light-emitting field-effect transistors, charge modulation spectroscopy

Their high ambipolar charge carrier mobilities combined with narrow emission bands in the near-infrared (nIR) make single-walled carbon nanotubes (SWCNTs) a promising material for applications in electrically driven light sources.¹⁻⁴ Due to advances in sorting techniques such as selective wrapping with conjugated polymers,⁵⁻⁷ it is now possible to prepare large amounts of chirality-pure SWCNT dispersions in organic solvents that are suitable for reproducible solution-processing of thin-films.⁸⁻¹¹ However, the progress in optoelectronic applications has been limited by the low luminescence efficiencies of SWCNT films (photoluminescence quantum yield ~0.1 %) and thin-film devices (external quantum efficiency < 0.01 %).^{2,3} These low emission efficiencies result from diffusion-limited exciton quenching, *e.g.*, at lattice defects or nanotube-nanotube junctions,¹² self-absorption due to a small Stokes shift,⁷ the presence of low-lying dark excitonic states,¹³ and Auger-type quenching by charges in devices.¹⁴⁻¹⁶ Likewise, defect-induced exciton-quenching has been shown to limit exciton transport and harvesting efficiency in photovoltaic cells based on bilayers of fullerenes and semiconducting SWCNT networks.¹⁷

Recently, the controlled functionalization of SWCNTs with luminescent sp^3 defects has emerged as a powerful approach to enhance their optical properties.¹⁸⁻²⁰ These quantum defects can be created through covalent binding of functional groups such as oxygen,²¹ alkyl,²² or aryl moieties²³ and act as efficient exciton traps. Optical trap depths are on the order of ~100 – 300 meV. They are partially determined by the chemical nature of the attached groups²² but more importantly by the defect binding configuration on the nanotube lattice.^{24, 25} Through exciton localization, these sp^3 defects prevent diffusion to quenching sites and give rise to red-shifted photoluminescence (PL) with long lifetimes.²⁶ They even enable high-purity single-photon emission at room temperature.²⁷ Combined with the chirality-dependent emission wavelengths of nanotubes, sp^3 functionalization allows the emission to be spectrally tuned across the nIR for potential

applications such as electrically pumped single-photon sources at telecommunication wavelengths.^{28, 29}

While the spectroscopic properties of sp^3 -functionalized SWCNTs have been extensively investigated, only very few studies were directed at the impact of functionalization on charge transport. Wilson *et al.* monitored the formation of sp^3 defects by measuring the resistance of electrically contacted, individual SWCNTs exposed to an aqueous diazonium salt solution.³⁰ In good agreement with quantum theoretical calculations,³¹ an average resistance increase of ~ 6 k Ω was attributed to the introduction of a single defect. Similarly, Bouilly *et al.* observed a conductance drop in single-nanotube transistors between ~ 20 % and two orders of magnitude depending on the number of sp^3 defects created by diazonium chemistry in patterned nanowells.³² Single-nanotube transistors with isolated sp^3 defects were further used as sensors by covalently attaching groups with specific binding motifs (*e.g.*, nucleic acid strands for DNA detection) and monitoring variations in the gating behaviour.^{32, 33}

Despite these advances, a comprehensive picture of charge transport in sp^3 -functionalized SWCNTs is still missing. This is mainly due to a lack of information on the investigated nanotube species, *i.e.*, their chirality or even their electronic type, in previous studies. Furthermore, in the absence of spectroscopic data, it was unclear whether or not the introduced defects were indeed luminescent exciton traps. Hence, the interaction of sp^3 defects and defect-localized excitons with charge carriers in active devices remains ambiguous. To the best of our knowledge, the impact of sp^3 functionalization on charge transport in semiconducting SWCNT networks that show excellent performances in field-effect transistors (FETs) has not been explored yet. A fundamental understanding of both their spectroscopic and electrical properties is, however, crucial to realize optoelectronic applications with sp^3 -functionalized SWCNT networks.

Here, we demonstrate ambipolar and light-emitting FETs based on networks of monochiral and sp^3 -functionalized (6,5) SWCNTs that show both high charge carrier mobilities and electroluminescence (EL) from the defect states. By employing EL, PL and charge-modulated PL spectroscopy in combination with temperature-dependent current-voltage measurements, we explore the interactions of sp^3 defects with charge carriers and their impact on charge transport through the network. We find that sp^3 defects act as shallow charge traps, from which carriers detrapp easily at room temperature. Thus, sp^3 -functionalized SWCNTs actively participate in charge transport through the network and contribute to the EL, allowing for the defect emission to be harnessed in nIR light-emitting devices.

RESULTS AND DISCUSSION

sp^3 Functionalization of (6,5) SWCNTs. We investigate highly purified semiconducting (6,5) SWCNTs as a model system to study the impact of sp^3 functionalization on charge transport through carbon nanotube networks. (6,5) SWCNT dispersions in toluene were obtained *via* shear force mixing and polymer-wrapping with the polyfluorene-bipyridine copolymer PFO-BPy (see **Figure 1a** and Methods).⁷ Raman and absorption spectra (Supporting Information, **Figure S1**) confirmed the absence of metallic and other minority SWCNTs in the dispersion. The controlled introduction of luminescent sp^3 defects to polymer-wrapped nanotubes in organic solvents was accomplished by a recently established reaction protocol (**Figure 1a**).³⁴ This method employs the phase-transfer agent 18-crown-6 to solubilize a pre-formed diazonium salt (here, 4-bromobenzenediazonium tetrafluoroborate) in a (6,5) SWCNT dispersion in toluene/acetonitrile (80:20 vol.-%, for details see Methods). After reacting for 16 hours at room temperature and in the dark, nanotubes were collected *via* filtration and thoroughly washed to remove unreacted

diazonium salt and reaction byproducts. Redispersion of the filter cake in a small volume of fresh toluene by bath sonication yielded concentrated dispersions suitable for spin-coating of dense SWCNT networks. Note that filtration and redispersion were similarly carried out before device processing for unfunctionalized (“pristine”) (6,5) SWCNTs to remove most of the excess wrapping polymer.

Upon covalent functionalization, a new emission band (E_{11}^*) appeared in the PL spectra of the SWCNT dispersions (E_{22} excitation at 575 nm) in addition to the E_{11} transition, as shown in **Figure 1b**. This additional peak originates from the radiative decay of excitons that are localized at symmetry-breaking sp^3 defects in the nanotube lattice.²³ For the bromoaryl defects employed here, the main defect PL peak occurred at ~1166 nm corresponding to a red-shift by ~174 meV from the mobile E_{11} exciton (~1002 nm). The sp^3 defect density on the (6,5) SWCNTs and thus intensity of the E_{11}^* emission was controlled by variation of the diazonium salt concentration in the reaction mixture (see **Figure 1b**). Higher concentrations resulted in higher E_{11}^*/E_{11} PL ratios. We estimate that the defect densities studied here range from approximately 5 to 30 defects per μm . For the highest degree of functionalization, an additional emission band (E_{11}^{*-}) - even further red-shifted than the dominant E_{11}^* transition - was observed in agreement with previous results.³⁴ This feature is attributed to a different defect binding configuration on the chiral (6,5) SWCNT lattice, resulting in deeper exciton traps as indicated by quantum mechanical calculations.^{35, 36}

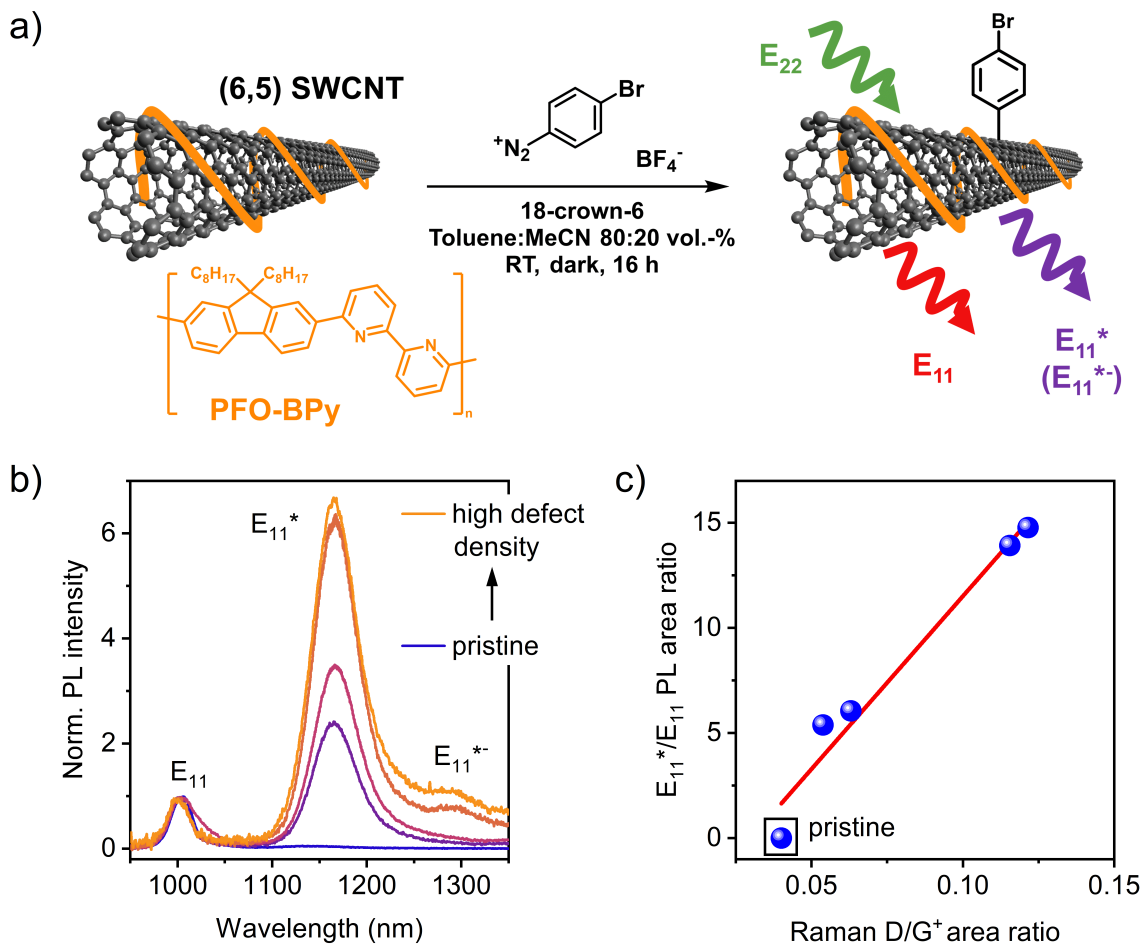


Figure 1. **a)** Reaction scheme for the controlled sp^3 functionalization of PFO-BPy-wrapped (6,5) SWCNTs with 4-bromobenzenediazonium tetrafluoroborate and schematic illustration of the PL properties of functionalized SWCNTs. After optical E_{22} excitation, red-shifted E_{11}^* and E_{11}^{*+} emission from defect-localized excitons is observed in addition to E_{11} emission. **b)** Normalized PL spectra of sp^3 -functionalized (6,5) SWCNT dispersions with different defect densities under pulsed excitation at the E_{22} transition (575 nm, $\sim 0.02 \text{ mJ cm}^{-2}$). **c)** Correlation between integrated PL ratio and Raman D/G^+ ratio and linear fit to the data.

The controlled variation of the defect densities was further corroborated by resonant Raman spectroscopy. An increasing ratio of the defect-related D mode to G⁺ mode Raman signal areas (Raman D/G⁺ area ratio) was observed with rising diazonium salt concentration and can be used as a metric for the number of sp³ defects in the nanotube lattice (Supporting Information, **Figure S2**). For the defect density range explored here, the integrated E₁₁*/E₁₁ PL ratio also correlated well with the Raman D/G⁺ ratio (**Figure 1c**). In addition, the recorded absorption spectra clearly showed the emergence of a E₁₁* defect state absorption band at ~1156 nm (Supporting Information, **Figure S3**) that increased with defect density. For further characterization, the Raman D/G⁺ ratio as well as the integrated E₁₁*/E₁₁ ratio of the absorption and PL spectra were used as metrics for the defect concentration.³⁴

Field-effect transistors with sp³-functionalized SWCNT networks. To investigate the properties of sp³-functionalized SWCNTs in active optoelectronic devices and to determine the impact of functionalization on charge transport (*e.g.*, scattering or trapping of charge carriers at the defects, as schematically illustrated in **Figure 2a**), we fabricated bottom-contact, top-gate field-effect transistors (FETs, see **Figure 2b** for schematic device layout) with interdigitated source/drain electrodes (channel length, $L = 20 \mu\text{m}$ and channel width, $W = 10 \text{mm}$), dense spin-coated layers of pristine and sp³-functionalized SWCNTs (see **Figure 2c** and Supporting Information, **Figure S4** for atomic force microscopy (AFM) images), a bilayer PMMA/HfO_x dielectric, and a silver top-gate electrode (see Methods section for details). All SWCNT networks were annealed in dry nitrogen at 150 °C to remove residual water and oxygen while avoiding detachment of covalently bound aryl groups above ~200 °C as recently shown by Schirowski *et al.*³⁷

Figure 2d shows the transfer characteristics in the linear regime (source-drain voltage $V_{ds} = -100$ mV) for a pristine SWCNT network FET and a device with an sp^3 -functionalized nanotube network with high defect density. Both clearly show ambipolar charge transport (*i.e.*, electron and hole conduction) with on/off current ratios on the order of $10^5 - 10^6$ and low gate leakage currents (< 1 nA). A significant decrease in both electron and hole currents and thus carrier mobility is evident for the highly functionalized SWCNT network FET in comparison to the pristine reference. Corresponding output characteristics as well as transfer curves for network FETs with all of the different defect densities are shown in the Supporting Information, **Figures S5, S6**. The slight current hysteresis in all transfer characteristics probably results from the relatively low annealing temperature and hence electron trapping by residual moisture,³⁸ which is also reflected in the lower electron currents compared to the hole currents even for pristine SWCNTs.

To evaluate the impact of sp^3 functionalization on the charge transport in these SWCNT networks, we first compare the maximum carrier mobilities in the linear regime. As shown in **Figure 2e**, the linear electron and hole mobilities gradually decrease with increasing defect density, here represented by the Raman D/G⁺ area ratio. Linear hole mobilities reached 5.0 ± 0.2 cm² V⁻¹ s⁻¹ for pristine and 1.7 ± 0.1 cm² V⁻¹ s⁻¹ for highly functionalized networks, whereas electron mobilities decreased from 1.2 ± 0.2 cm² V⁻¹ s⁻¹ (pristine) to 0.4 ± 0.04 cm² V⁻¹ s⁻¹ (highest defect density). Note that for functionalized networks higher gate voltages had to be applied to reach the maximum transconductance and thus charge carrier mobility (see Supporting Information, **Figure S5b**). **Figure 2f** shows the decrease of hole and electron mobilities normalized to the pristine reference. Both drop to roughly one third of the initial value for the highest defect concentration with a Raman

D/G⁺ area ratio of 0.12 and with an E₁₁^{*}/E₁₁ PL ratio of ~15 in dispersion (see Supporting Information, **Figure S7** for absolute and normalized mobilities vs. various defect metrics).

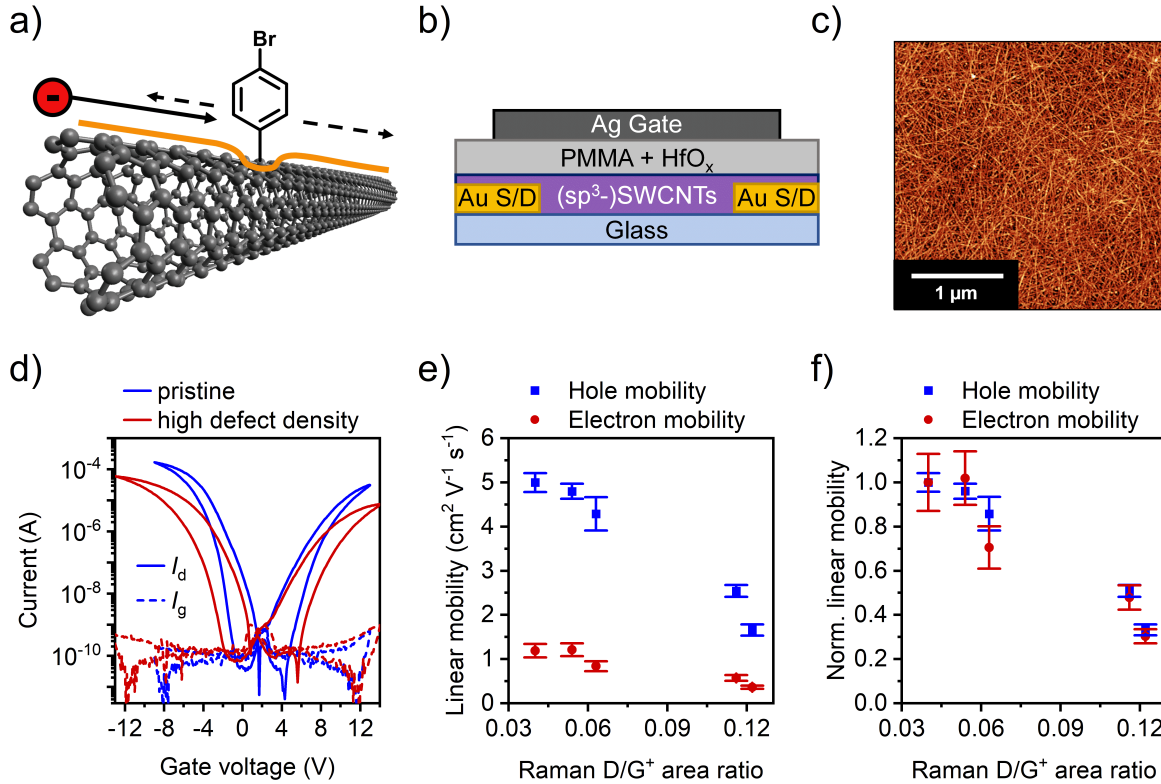


Figure 2. **a)** Schematic illustration of charge transport through sp^3 -functionalized SWCNTs. Defects may act as scattering sites or trap states for charge carriers. **b)** Schematic device architecture of bottom-contact, top-gate SWCNT network FETs. **c)** Atomic force micrograph (scalebar, 1 μm) of a representative, dense network of sp^3 -functionalized (6,5) SWCNTs. **d)** Ambipolar transfer characteristics (source-drain voltage $V_{\text{ds}} = -100$ mV, $L = 20$ μm , $W = 10$ mm) of FETs with networks of pristine (blue) and sp^3 -functionalized (6,5) SWCNTs (red). Solid lines are drain currents, I_{d} , dashed lines are gate leakage currents, I_{g} . **e)** Absolute and **f)** normalized linear charge carrier mobilities (holes, blue squares; electrons, red circles) of pristine and sp^3 -functionalized (6,5) SWCNT FETs vs. Raman D/G⁺ area ratio.

Frequency-dependent capacitance measurements further showed a decrease in the FET cut-off frequency with increasing degree of functionalization, mainly reflecting the lower carrier mobilities of the network (Supporting Information, **Figure S8**). The static capacitances of all network FETs, as extracted from capacitance-voltage sweeps, were very similar (Supporting Information, **Table S1**), confirming similar network densities that were also well above the limit for mobility saturation.³⁹ Hence, any observed differences in electrical performance can be attributed directly to the different sp^3 defect densities.

As shown above, even at the highest level of sp^3 functionalization studied here, the SWCNT network FETs remain fully operational and still exhibit surprisingly high ambipolar carrier mobilities. In previous reports, the introduction of a single sp^3 defect on an individual semiconducting nanotube already resulted in a conductance drop of $\sim 20\%$.^{30, 32} However, in single-nanotube devices, charge carriers are forced to pass sp^3 defects, whereas this is not necessarily the case in random nanotube networks with multiple possible conduction pathways. This difference raises fundamental questions about the charge transport mechanisms in functionalized SWCNT networks: First, what is the nature of sp^3 defects with respect to charge transport along one nanotube (scattering site, shallow or deep trap state)? And second, do sp^3 -functionalized SWCNTs still actively participate in charge transport or are nanotube segments with defects bypassed in a dense network? The latter would result in lower overall mobilities simply due to fewer available current pathways but would also reduce possible electroluminescence from defect sites. These scenarios directly affect the application potential of sp^3 -functionalized SWCNT networks for electroluminescent devices. They will be addressed in the following by comparing electroluminescence measurements, static gate voltage-dependent photoluminescence, charge

modulation photoluminescence spectroscopy, and temperature-dependent transport measurements of pristine and functionalized (6,5) SWCNT network FETs.

Electroluminescence from sp^3 defect sites. To investigate the charge transport pathways through networks of pristine and sp^3 -functionalized (6,5) SWCNTs, we employed electroluminescence (EL) measurements in the near-infrared. The injection, transport and recombination of holes and electrons in the ambipolar regime leads to the generation of excitons and thus light emission,⁴⁰ as schematically illustrated in **Figure 3a**. EL is observed from a narrow recombination zone that is formed where the hole and electron accumulation layers meet in the channel. Since EL correlates directly with current density, its spatial and spectral resolution has been previously utilized to analyze charge transport through mixed-chirality SWCNT networks *via* the bandgap-dependent current shares,^{15, 16} and to visualize patterned current pathways in photoswitchable SWCNT network FETs.⁴¹ Here, we use the spectral signatures of sp^3 defects (E_{11}^*) and mobile excitons (E_{11}) to study the contribution of functionalized nanotubes to charge transport in the networks.

First, we imaged the near-infrared EL from these FETs with a 2D-InGaAs camera (800 – 1600 nm) during a constant current sweep ($I_d = -100 \mu\text{A}$) in the ambipolar regime. **Figure 3b** shows a homogeneous recombination and emission zone within the channel ($L = 20 \mu\text{m}$) of a sp^3 -functionalized SWCNT FET. This narrow emission zone (width 1 – 2 μm) extended without interruption along the entire channel width and could be arbitrarily positioned between source and drain electrodes by adjusting the gate voltage. Adding up a large number of such images for a complete gate voltage sweep yields a composite EL image (see **Figure 3c**) that reflects the current density distribution within the channel.^{41, 42} No preferential transport paths were observed on the length scale of this diffraction-limited imaging method.

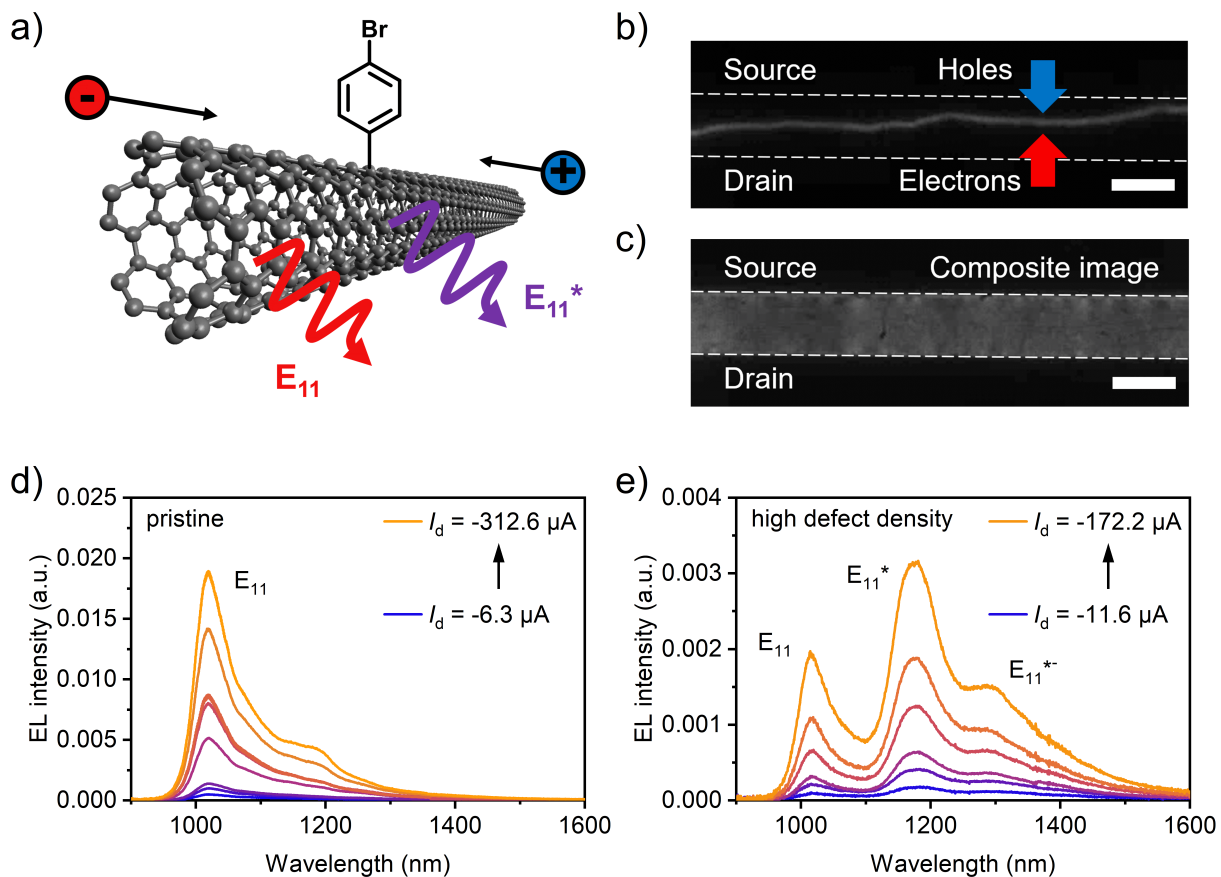


Figure 3. **a)** Schematic illustration of electroluminescence from sp^3 -functionalized SWCNTs through ambipolar carrier recombination of thermalized holes and electrons. **b)** Near-infrared EL image of the channel ($L = 20 \mu\text{m}$) of an sp^3 -functionalized SWCNT network FET, showing a homogeneous recombination and emission zone when the device is biased in the ambipolar regime (drain current $I_d = -100 \mu\text{A}$). **c)** Composite EL image for a full gate voltage sweep at a constant current ($I_d = -100 \mu\text{A}$), showing homogeneous EL emission from the entire channel area (scalebars, $20 \mu\text{m}$). **d, e)** Representative EL spectra of pristine and sp^3 -functionalized (high defect density) SWCNT network FETs in the ambipolar regime for different drain currents.

We then resolved the EL spectrally with the emission zone always positioned in the center of the channel (as in **Figure 3b**) for different drain currents. Note that changing the drain current while keeping the position of the emission zone in the center of the channel requires changing both the gate voltage V_g and the source-drain voltage V_{ds} . **Figure 3d** shows the EL spectra of a pristine SWCNT network transistor. In addition to the E_{11} emission, the spectra exhibit a prominent tail toward longer wavelengths that can be attributed to typical SWCNT emission side bands.^{43, 44} Trion emission at ~ 1180 nm, which is strong in electrolyte-gated SWCNT FETs,⁴⁵ is rather weak here, probably due to the significantly lower carrier densities. As expected, the emission intensity increased nearly linearly with the drain current. Maximum EL emission efficiencies of ~ 0.015 % were obtained for these pristine SWCNT networks.

For FETs with sp^3 -functionalized SWCNTs, electrically induced emission from the sp^3 defects is clearly observed (see **Figure 3e**). As shown in the Supporting Information, **Figure S9**, the defect state EL is tunable in intensity and increases with the level of functionalization. At the highest defect density, about 80 % of emission comes from sp^3 defects. Although we observed a slight increase in EL emission efficiencies for low defect densities, they largely remained within the same range as the unfunctionalized SWCNT network devices and slightly decreased for the highest defect densities as expected. The spectral shape of the EL was also essentially independent of the position of the emission zone within the transistor channel, even at the electrodes. Normalizing the EL spectra to the E_{11} exciton signal confirms that the defect emission is stable over 1 – 2 orders of magnitude in current density, which should be beneficial for applications (Supporting Information, **Figure S10**). Only a slight decrease in the E_{11}^*/E_{11} peak ratio was observed for increasing drain current (and applied gate voltage) for all functionalized networks.

Nevertheless, the ratio of defect-to- E_{11} electroluminescence was significantly lower than the PL ratio in the original dispersion (see **Figure 1b**). One possible cause might be different excitation densities and thus state-filling of exciton traps, which is well-known from the PL spectra of sp^3 -functionalized SWCNTs. The defect emission shows earlier saturation compared to the mobile E_{11} excitons for increasing pump power.^{34,46} However, a plot of the integrated EL intensities vs. drain currents on a log-log scale yields slopes of ~ 1 for both the defect and E_{11} emission peaks (Supporting Information, **Figure S11a**), which confirms that the data was collected in the linear excitation regime without significant state-filling. This notion is further supported by the relatively low exciton densities (for details and calculations see the Supporting Information) that are estimated for EL at the given current densities. Additionally, a PL spectrum acquired from the channel region under non-resonant, low-power continuous wave (cw) excitation displays very similar E_{11}^*/E_{11} peak ratios (Supporting Information, **Figure S11b**). The lower defect emission intensity appears to be mainly associated with film formation.

Interestingly, emission from the even further red-shifted E_{11}^{*-} defects, which originate from a different defect binding configuration, is more prominent in the EL spectra of highly functionalized SWCNT networks compared to the PL spectrum. The ultrafast exciton transfer within nanotube films⁴⁷ should affect both EL and PL spectra in a similar fashion. To address this question, an investigation of the emission properties of SWCNT networks with both E_{11}^* and E_{11}^{*-} defects at similar densities, as can be created by a recently reported base-promoted functionalization method,²⁵ would be useful but is beyond the scope of the current study.

Note that the sp^3 defect EL observed here originates from the recombination of thermalized electrons and holes and not from impact excitation as shown recently by Xu *et al.*⁴⁸ Our results demonstrate that sp^3 -functionalized SWCNTs can be integrated in multi-functional devices such

as light-emitting FETs, where they support ambipolar charge transport and exhibit electroluminescence. The observation of defect emission indicates that electron-hole recombination occurs near (within the exciton diffusion length) or at defect sites and hence charge transport must at least partially go through segments of nanotubes bearing sp^3 defects. The similarity of the EL and PL spectrum of functionalized SWCNT networks at low excitation densities suggests that there are no preferential transport paths or recombination sites.

Static, gate-voltage dependent photoluminescence. A more detailed analysis of photoluminescence in FETs should help to elucidate the interaction between excitons and charge carriers in sp^3 -functionalized SWCNT networks and their impact on emission properties. We performed static, gate voltage-dependent PL measurements under non-resonant cw excitation (785 nm) in the linear excitation regime (**Figure 4** and Supporting Information, **Figure S12**) as well as under pulsed E_{22} excitation (Supporting Information, **Figures S13, S14**). In the latter case, the relative E_{11}^* and E_{11}^{*-} peak intensities were considerably lower due to the much higher exciton densities (about two orders of magnitude, for details see the Supporting Information) leading to state filling.^{34, 46}

All gate voltage-dependent PL spectra show a decrease of the emission intensities (E_{11} , E_{11}^* , E_{11}^{*-}) with increasing carrier density (holes or electrons) due to Auger-type quenching of excitons with charges (for PL spectra in hole accumulation see **Figure 4a**).⁴⁹ However, quenching of the defect PL is more efficient than that of the E_{11} emission, as shown in the normalized spectra in **Figure 4b**. This trend is analogous to the EL spectra, where the E_{11}^*/E_{11} ratio also decreases slightly for increasing current densities.

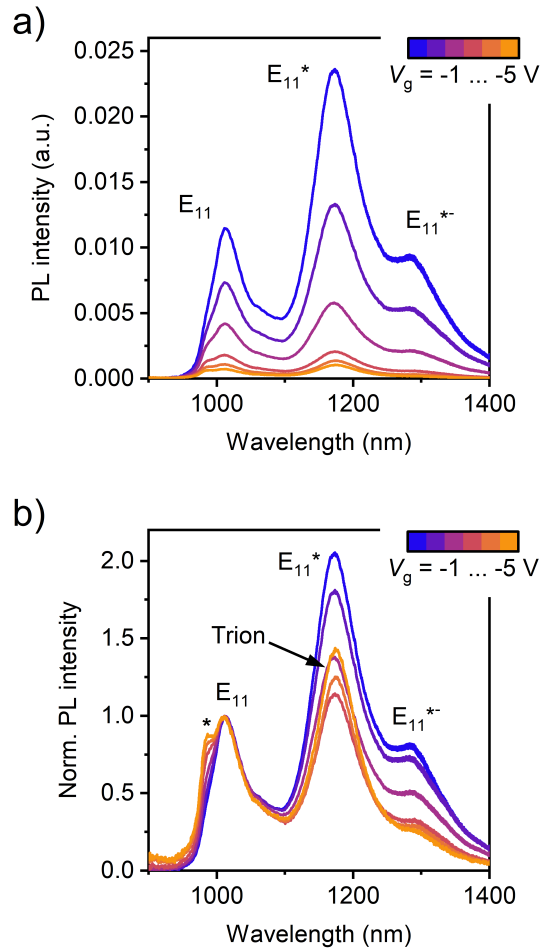


Figure 4. a) Static, gate voltage-dependent PL spectra (source-drain voltage $V_{ds} = -10$ mV) of sp^3 -functionalized SWCNT network transistors ($L = 20$ μm) with high defect density in hole accumulation. Spectra were acquired from the middle of the channel under non-resonant continuous wave excitation (785 nm, ~ 320 W cm^{-2}). **b)** Normalized PL spectra show that E_{11}^* and E_{11}^{*+} defect PL is more efficiently quenched than the E_{11} emission when gate voltages are applied. At high V_g , PL from positively charged triions can be observed at very similar wavelengths to the E_{11}^* emission. Note that the peak at ~ 985 nm marked with an asterisk corresponds to the Raman 2D mode of (6,5) SWCNTs.

Previous studies by Shiraishi *et al.* on PL from electrochemically doped oxygen- and aryl-functionalized (6,5) SWCNT films revealed a similar effect and allowed them to determine redox potentials corresponding to the highest occupied molecular orbital (HOMO) and lowest unoccupied molecular orbital (LUMO) levels as well as the electrochemical bandgap of the defect sites.^{50,51} For bromoaryl defects (as used here) the electrochemical bandgap was ~ 53 meV smaller for E_{11}^* compared to E_{11} (HOMO level shifted by ~ 31 meV to higher energies, LUMO level shifted by ~ 22 meV to lower energies), suggesting that these sp^3 defects act as shallow charge carrier traps that would enable detrapping at room temperature (thermal energy ~ 25 meV). Charges that preferentially reside at the sp^3 defects may explain the predominant quenching of E_{11}^* excitons and thus the decrease of the E_{11}^*/E_{11} ratio in PL and EL spectra with increasing hole or electron density.

Further evidence is provided by pump power-dependent PL measurements under cw excitation (Supporting Information, **Figures S15, S16**). The integrated E_{11}^*/E_{11} and E_{11}^*/E_{11} PL intensity ratios show that the saturation of defect emission occurs at higher excitation powers when a gate voltage ($V_g = -2$ V, hole accumulation) is applied compared to the neutral state ($V_g = 0$ V). Charge carriers residing in close proximity to the defect sites should lead to a shortening of localized-exciton lifetimes through non-radiative quenching. Hence, state-filling, which is commonly attributed to the long lifetime of sp^3 defect-localized excitons and fast exciton diffusion to defect sites,⁴⁶ is reduced and becomes significant only at higher excitation densities. Unfortunately, a quantitative evaluation of the PL spectra with regard to the defect-to- E_{11} emission ratio depending on the carrier density (gate voltage) is hindered by the additional contribution of trion emission at very similar wavelengths (~ 1175 nm) to the E_{11}^* peak (~ 1173 nm) (Supporting Information, **Figures S12-S14**).

Overall, the gate voltage-dependent PL data suggest a certain degree of charge localization at the sp^3 defects within the SWCNT networks. Due to the static nature of both EL and PL spectroscopy, the observed dependencies could result from either mobile or trapped charge carriers. To unambiguously investigate the interaction of sp^3 defects in (6,5) SWCNTs with mobile charge carriers, a dynamic measurement such as modulation spectroscopy is required.

Charge modulation PL spectroscopy. Charge modulation spectroscopy (CMS) is a dynamic and highly sensitive method that has been widely used to investigate charge transport in organic semiconductors.^{52,53} We recently applied this technique to SWCNT network FETs and introduced charge modulation PL (CMPL) spectroscopy as a complementary approach to probe the mobile charge carriers in SWCNT networks.⁵⁴ In CMPL, a sinusoidal voltage (peak-to-peak voltage V_{pp}) is applied to the gate electrode (which is at a constant offset voltage V_{os}) while the semiconducting layer is excited by a laser. The differential change in PL (ΔPL) upon modulation of charge carrier density in the transistor channel is recorded with a lock-in detection scheme. The detected signal correlates exclusively with mobile charge carriers because charges in deep trap states cannot be modulated. A schematic of the setup is shown in the Supporting Information, **Figure S17**.

Figure 5a shows the CMPL spectra for a pristine (6,5) SWCNT network at different V_{os} (modulation frequency $f = 363$ Hz, $V_{pp} = 0.2$ V). In agreement with previous results, the signal attributed to E_{11} exciton quenching initially increases with V_{os} due to the increase in capacitance and higher modulated carrier density.⁵⁴ At approximately -1.3 V, the ΔPL signal passes through a maximum and decreases again for higher V_{os} . Since the offset voltage V_{os} corresponds to the static charge carrier density in the channel, on which the modulation is superimposed, this decrease can be attributed to static exciton quenching (see the static voltage-dependent PL spectra).

Consequently, the effect of charge modulation becomes less significant for high V_{os} and because only the differential change is recorded in CMPL, the signal decreases. Spectra normalized to the E_{11} peak are essentially identical (Supporting Information, **Figure S18a**).

Variation of the modulation frequency was used to probe the temporal response of charge carriers to the sinusoidal bias. Since the carrier mobilities in the investigated gate voltage range are still low (Supporting Information, **Figure S5b**), charges cannot fully follow high modulation frequencies and the signal intensity decreases with increasing frequency (Supporting Information, **Figure S18b**). The normalized spectra, however, are nearly identical (Supporting Information, **Figure S18c**), confirming that all contributions to the spectrum arise from the same physical effect, that is, quenching by mobile charges. Modulated PL spectra with good signal-to-noise ratios were obtained for frequencies as high as 10 kHz which is in good agreement with the cut-off frequencies observed in the capacitance measurements of the FETs (Supporting Information, **Figure S8**).

For sp^3 -functionalized SWCNT networks, the voltage-dependent CMPL spectra closely resemble the static PL spectra, exhibiting signals corresponding to the modulation of E_{11} and sp^3 defect emission. **Figure 5b** shows the CMPL spectra for a high defect density sample, where the peaks at ~ 1172 nm and ~ 1290 nm are assigned to the E_{11}^* and E_{11}^{*-} transitions, respectively. Importantly, as CMPL features are attributed to the PL modulation by mobile carrier density, this observation corroborates that sp^3 -functionalized SWCNT segments in a network are indeed sampled by mobile carriers. This notion is further supported by frequency-dependent CMPL measurements that showed modulation of defect PL emission even at frequencies of ~ 8 kHz (Supporting Information, **Figure S19**). The near-identical normalized spectra confirm that all spectral contributions have a common physical origin, that is, quenching by mobile charges.

Voltage- and frequency-dependent CMPL spectra of sp^3 -functionalized SWCNT network FETs with a low defect density also follow these trends (Supporting Information, **Figure S20**).

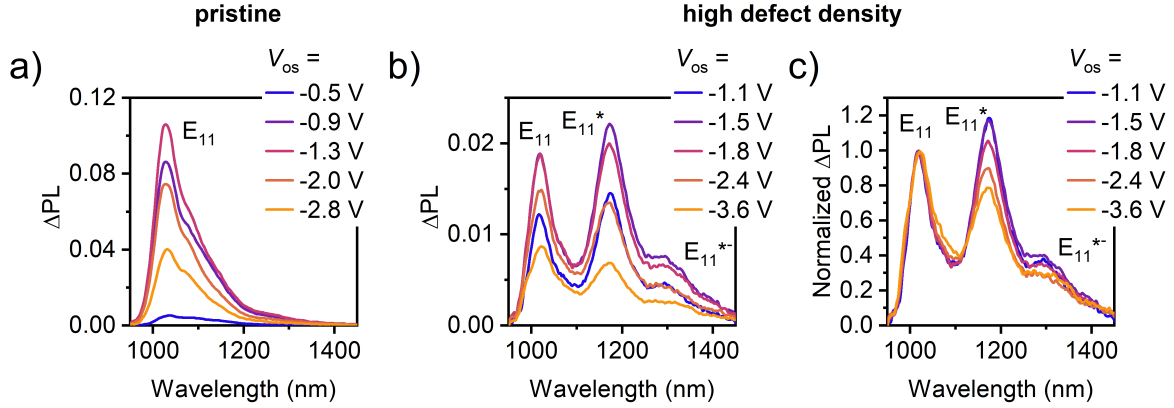


Figure 5. **a)** Voltage-dependent CMPL spectra of pristine (6,5) SWCNT network, showing an initial increase and subsequent decrease of the E_{11} ΔPL signal with V_{os} . **b)** Voltage-dependent CMPL spectra of a sp^3 -functionalized SWCNT network with high defect density, showing PL modulation of mobile (E_{11}) as well as defect-localized (E_{11}^* , E_{11}^{*-}) excitons. **c)** CMPL spectra normalized to the ΔPL signal of E_{11} . All spectra were acquired from the middle of the channel ($L = 20 \mu\text{m}$) at a modulation frequency $f = 363 \text{ Hz}$ and $V_{pp} = 0.2 \text{ V}$.

Normalized CMPL spectra of FETs with functionalized (6,5) SWCNTs (**Figure 5c**) show a decrease in E_{11}^*/E_{11} signal intensity with increasing charge carrier density (*i.e.*, V_{os}). This decrease is similar to the static voltage-dependent PL spectra (Supporting Information, **Figure S12**) and also suggests that the sp^3 defects are lower-lying electronic states that participate in the charge transport through the networks. With increasing static carrier density, these shallow trap states are filled and thus cannot be fully modulated anymore.

At first glance, this picture seems to contradict the frequency-dependent data, which suggest that charge carriers are highly mobile on SWCNT segments with sp^3 defects under the measurement conditions. No CMPL response would be expected for carriers in deep trap states or at least some differences should appear in the temporal response at higher modulation frequencies. However, modulation spectroscopy is able to probe shallow traps as long as they can be filled and emptied on the timescale of charge modulation.⁵³ Short detrapping times at room temperature could thus explain this observation. Analogous to He *et al.* who calculated the thermal detrapping rates for excitons localized at sp^3 defects,⁵⁵ we estimate the thermal detrapping rate constant (k) for charge carriers using the Arrhenius equation $k = A \cdot \exp\left(-\frac{E_a}{k_B T}\right)$. Based on transition state theory, the preexponential factor can be written as $A = k_B T/h$ (with k_B – Boltzmann constant, T – temperature, h – Planck constant). Assuming a trap depth of ~ 25 meV, we find detrapping times on the order of ~ 1 ps at 300 K, which is orders of magnitude faster than the voltage modulation in CMPL ($\sim 10^3$ – 10^4 Hz). Even assuming the optical trap depths of ~ 175 meV (E_{11}^*) and ~ 255 meV (E_{11}^{*-}) still results in estimated detrapping times of ~ 100 ps to few ns. Lowering the temperature could lead to slower detrapping and might eventually result in changes in the modulation spectra, as shown for organic semiconductors in low-temperature CMS experiments.^{53, 56} However, this experiment was not possible in our current CMPL setup.

Temperature-dependent charge transport. The data discussed so far have shown that sp^3 defects lead to red-shifted electroluminescence from SWCNT networks but also impede charge transport to some degree. Modulation spectroscopy at room temperature indicates that the defects are sampled by mobile carriers while acting as shallow traps, from which charges can detrap quickly at room temperature. The presence of such shallow trap states should be reflected in changes in

the subthreshold regime of the linear transfer characteristics of network FETs even at ambient temperatures. Indeed, as shown in the Supporting Information, **Figure S21**, the subthreshold slope at 300 K was lower for the sp^3 -functionalized SWCNT network transistors compared to the pristine (6,5) SWCNT FETs. We calculated the nominal trap densities from the subthreshold swing according to Kalb *et al.*⁵⁷ (see Supporting Information, **Table S2**). They are on the order of $10^{12} \text{ cm}^{-2} \text{ eV}^{-1}$ for the pristine (6,5) SWCNT networks as shown previously.⁵⁸ Upon functionalization, trap densities for electrons and holes increased by 50 – 60 %, indicating a noticeable but still moderate impact of the introduced sp^3 defects.

Temperature-dependent current-voltage measurements are a common tool to investigate charge transport in semiconductors in general and in semiconducting carbon nanotube networks in particular.⁵⁹⁻⁶¹ Shallow traps should have a larger effect at lower temperatures when detrapping is slowed down. For this purpose, FETs including two additional voltage probes in the channel were fabricated from the same SWCNT dispersions as discussed above to perform gated four-point-probe transport measurements (see Supporting Information, **Figure S22** for device architecture and measurement principle). This technique allows us to separate the temperature-dependent contact resistance from the channel resistance and thus to determine actual carrier mobilities in the nanotube network. This correction for contact resistance leads to a noticeable increase of the apparent network mobilities by 20 – 90 %. Hence, all of the following carrier mobilities are contact resistance-corrected.^{61, 62}

To assess the temperature dependence of the network mobilities, transfer characteristics in the linear regime ($V_{ds} = -100 \text{ mV}$) were recorded from 300 K down to 25 K (see **Figure 6a** with only every other transfer curve shown) for a pristine (6,5) SWCNT network and for devices with low and high sp^3 defect densities. Note that different gate voltage ranges were used for

unfunctionalized and functionalized samples to reduce hysteresis while still covering the full accumulation range. The on-currents monotonously increased with temperature, corroborating thermally activated charge transport in all networks as reported before.^{61, 63} Due to shifts of the onset voltages V_{on} with temperature, the contact resistance-corrected mobilities were extracted at a fixed gate voltage overdrive ($V_{\text{g}} - V_{\text{on}}$) of ± 6 V for electrons and holes, respectively, and thus at similar carrier concentrations ($\sim 4 \cdot 10^{12} \text{ cm}^{-2}$).

Temperature-dependent mobilities normalized to the respective value at 300 K are shown in **Figure 6b** for holes and electrons (for absolute values see Supporting Information, **Figure S23**). The logarithmic plots vs. $1/T$ show pronounced differences between pristine, low defect density and high defect density SWCNT networks in the low-temperature range, but a very similar behavior at higher temperatures. These differences are also observed when comparing the maximum mobilities.

The variable range hopping (VRH) model, which was developed to describe charge transport by hopping in disordered semiconductors,⁶⁴ clearly does not fit to the data especially for low temperatures. The fluctuation-induced tunneling (FIT) model would give better fits and is more commonly used.⁶⁵ However, the corresponding fit results depend strongly on the starting values and are rather difficult to compare. In any case, both models associate the temperature dependence of the carrier mobilities only with thermally activated carrier hopping across nanotube-nanotube junctions and neglect the contribution of intra-nanotube transport, which is proportional to $1/T$ for pristine SWCNTs.⁶⁶ We presume that the nanotube-nanotube junctions are unlikely to be directly affected by sp^3 defects at the low densities considered here with fewer than 3 defects per 100 nm (see above). If this assumption is correct, the observed differences between the absolute network mobility values and their temperature dependence must be caused by changes in the intra-nanotube

conductance, further supporting the idea that charge transport in SWCNT networks is not solely limited by the junctions but represents a superposition of intra- and inter-nanotube contributions.⁶³ Note that the impact of sp^3 defects on nanotube bundling and electrical contact within bundles remains unclear. However, due to the small size of the bromoaryl moieties compared to the fluorene units with the octyl sidechains of the PFO-BPy wrapping polymer and the low defect densities, a significant effect seems unlikely.

Even without an analytical model combining intra- and inter-nanotube contributions, we can compare the relative differences in temperature dependence of the mobility data in **Figure 6b**. At higher temperatures, thermally activated hopping across the nanotube-nanotube junctions is the dominating process for carriers moving through the networks. Assuming that the junctions are not directly affected by low-level sp^3 functionalization, the impact of additional shallow trap states on the temperature dependence is expected to be low. This notion is confirmed by the nearly identical slopes of the logarithmic mobilities *vs.* $1/T$ at temperatures above 150 K. However, for both hole and electron mobilities, the temperature dependence becomes stronger with defect density in the low-temperature range (< 150 K) where charge transport is dominated by tunneling between conductive nanotube segments. As tunneling is independent of temperature, the impact of intra-nanotube transport on the overall network mobility and consequently the impact of the sp^3 defects as shallow charge traps should be significant in this temperature range as clearly shown in **Figure 6b**. These data further support the hypothesis that both inter- and intra-nanotube contributions play a significant role for the overall network mobility. If the junction resistances were the only limiting factor for charge transport through the networks, no or only minor differences in the temperature dependence would be observed upon sp^3 functionalization.

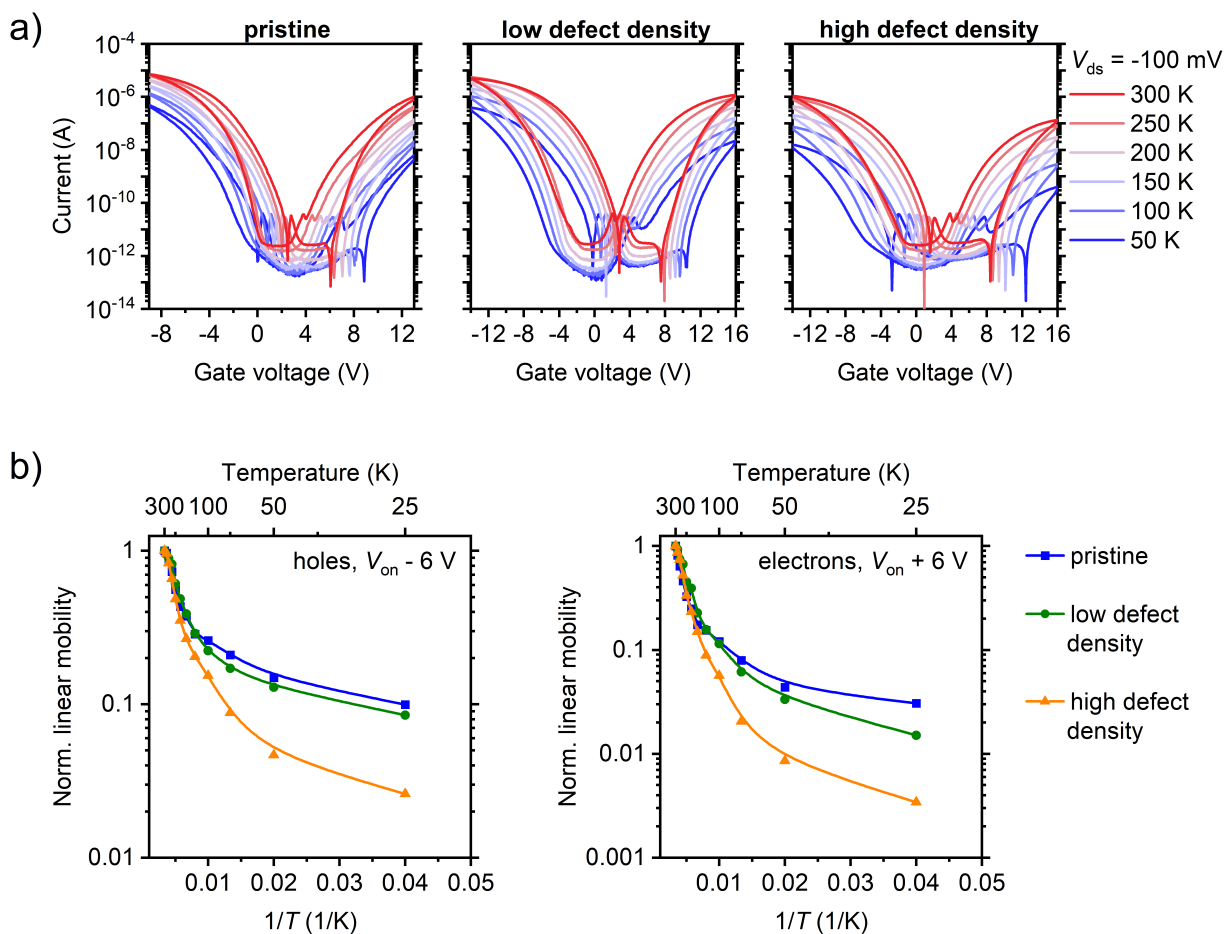


Figure 6. a) Temperature-dependent transfer characteristics (four-point probe geometry, $L = 40$ μm , $W = 1$ mm, source-drain voltage $V_{ds} = -100$ mV) of pristine and sp^3 -functionalized SWCNT network FETs between 25 – 300 K (only every other curve is shown). **b)** Temperature-dependent charge carrier mobilities for holes and electrons normalized to the values at 300 K. For better comparison, all mobilities were contact resistance-corrected and extracted at a fixed gate voltage overdrive of ± 6 V for electrons and holes, respectively. Lines are guides to the eye.

The absolute mobility values also decrease with increasing sp^3 defect density as shown in **Figure 2e** and Supporting Information, **Figure S23**. Since EL and CMPL measurements indicate

that functionalized SWCNT segments are sampled by mobile carriers and contribute to charge transport within the networks, we associate this decrease in mobility directly with increased resistance along individual SWCNTs due to defects rather than a reduction in the number of available current pathways in a dense nanotube network. Electrical measurements on a large number of devices with individual functionalized (6,5) nanotubes (similar to the experiments by Bouilly *et al.*³²) or short-channel transistors with aligned arrays of functionalized SWCNTs could remove the question of junction resistance. Furthermore, complementary methods such as microwave conductivity measurements⁶⁷ or THz spectroscopy⁶⁸ would be highly suitable for a contact-free and quantitative determination of intrinsic charge carrier mobilities. A combination of these techniques will be required to unambiguously separate the contributions of sp^3 defects and SWCNT junctions to charge transport in functionalized SWCNT networks.

CONCLUSION

We have demonstrated ambipolar and light-emitting field-effect transistors based on networks of polymer-sorted (6,5) SWCNTs with different densities of luminescent sp^3 defects that were introduced by diazonium chemistry and led to red-shifted E_{11}^* and E_{11}^{*-} emission. The covalent functionalization of the nanotubes resulted in a moderate, yet gradual decrease of hole and electron mobilities with increasing defect density, thus providing evidence that sp^3 defects may act as shallow charge traps that have a noticeable effect on charge transport especially at low temperatures (< 150 K). At room temperature, however, charges can be detrapped fast, and charge modulation PL spectroscopy corroborated that functionalized SWCNT segments are sampled by mobile carriers and actively participate in charge transport through the network. Importantly, even at high defect densities, the FETs remained fully operational and exhibited EL from the defect

states *via* ambipolar carrier recombination. The contribution of sp^3 defect emission (mostly E_{11}^*) to electroluminescence was tunable through the defect concentration and stable over a wide range of current densities. As the emission spectrum of the sp^3 -functionalized SWCNT network should be very narrow for electrically driven light-emitting devices, the selective introduction of only E_{11}^* defects would be highly beneficial for this purpose.²⁵ Using these defects with a different binding configuration and a deeper exciton trapping potential could also shift the EL spectrum even further toward application-relevant telecommunication wavelengths. Overall, the successful integration of sp^3 -functionalized semiconducting SWCNT networks into electroluminescent devices may enable applications that require both high carrier mobilities and controllable emission properties, such as electrically pumped single-photon sources in the nIR.

METHODS

Preparation of (6,5) SWCNT Dispersions. Nearly monochiral (6,5) SWCNT dispersions were obtained from CoMoCAT raw material (CHASM Advanced Materials Inc., Charge No. SG65i-L58, 0.38 g L⁻¹) *via* shear force mixing (Silverson L2/Air mixer, 10230 rpm, 72 h) and polymer-wrapping with poly[(9,9-dioctylfluorenyl-2,7-diyl)-*alt*-(6,6'-(2,2'-bipyridine))] (PFO-BPy, American Dye Source, $M_w = 40 \text{ kg mol}^{-1}$, 0.5 g L⁻¹) in toluene as described previously.⁷ The resulting dispersion was centrifuged twice for 45 min at 60000g (Beckman Coulter Avanti J26XP centrifuge) and filtered through a polytetrafluoroethylene (PTFE) syringe filter (pore size 5 μm) to remove aggregates.

sp³ Functionalization of (6,5) SWCNTs. sp³ Functionalization of PFO-BPy-wrapped (6,5) SWCNTs was performed according to the protocol introduced by Berger *et al.*³⁴ Briefly, SWCNTs (0.72 mg L⁻¹, corresponding to an optical density of 0.4 cm⁻¹ at the E₁₁ transition) were functionalized with 4-bromobenzenediazonium tetrafluoroborate in an 80:20 vol-% toluene/acetonitrile (MeCN) mixture. To increase the solubility of the diazonium salt, a solution of 18-crown-6 in toluene was added to the (6,5) SWCNT dispersion as a phase-transfer agent (concentration in the final reaction mixture, 7.6 mmol L⁻¹). After adding an appropriate amount of the diazonium salt in acetonitrile (concentrations in the final reaction mixture ranging between 0.3 mg mL⁻¹ and 2 mg mL⁻¹), the reaction was allowed to proceed at room temperature and in the dark for ~16 h. Then, the mixture was filtered through a PTFE membrane filter (Merck Millipore JVWP, pore size 0.1 μm) and the filter cake was washed with MeCN and toluene to remove unreacted diazonium salt, reaction byproducts, and excess polymer.

Device Fabrication. Bottom contact electrodes (interdigitated electrodes with $L = 20 \mu\text{m}$, $W = 10 \text{ mm}$ and four-point probe geometry with $L = 40 \mu\text{m}$, $W = 1 \text{ mm}$) were patterned by photolithography (double-layer LOR5B/S1813 resist, microresist technology GmbH) and electron beam evaporation of chromium (2 nm) and gold (30 nm) on glass substrates (Schott AG, AF32eco, 300 μm thickness). After lift-off in *N*-methyl pyrrolidone (NMP), substrates were cleaned by ultrasonication in acetone and 2-propanol for 10 min each. Filter cakes of pristine and functionalized SWCNTs were redispersed in fresh toluene by bath sonication for 30 min and the resulting dispersions were spin-coated ($3 \times 70 \mu\text{L}$, 2000 rpm, 30 s) onto the electrodes with annealing steps (100 °C, 2 min) in between. After rinsing with tetrahydrofuran and 2-propanol to remove residual polymer, SWCNT networks were patterned using photolithography as described above, oxygen plasma treatment (Nordson MARCH AP-600/300, 100 W, 120 s), and lift-off in NMP to remove all SWCNTs outside the channel area. The samples were annealed at 150 °C for 30 min in dry nitrogen atmosphere. As hybrid gate dielectric, ~11 nm of poly (methyl methacrylate) (PMMA, Polymer Source, $M_w = 315 \text{ kg mol}^{-1}$, syndiotactic) were spin-coated (80 μL , 4000 rpm, 60 s) from a solution in *n*-butyl acetate (6 g L⁻¹), followed by deposition of ~61 nm hafnium oxide (HfO_x) *via* atomic layer deposition (Ultratech Inc., Savannah S100) at a temperature of 100 °C using a tetrakis(dimethylamino)hafnium precursor (Strem Chemicals Inc.) and water as the oxidizing agent. Thermal evaporation of 30 nm silver top gate electrodes through a shadow mask completed the devices.

Characterization. Baseline-corrected absorbance spectra of SWCNT dispersions were recorded with a Cary 6000i UV-vis-nIR spectrometer (Varian Inc.). A Renishaw inVia confocal Raman microscope in backscattering configuration equipped with a 50 \times long working distance objective (Olympus, N.A. 0.5) was used for acquisition of Raman spectra (532 nm excitation wavelength).

Atomic force micrographs were acquired with a Bruker Dimension Icon in the ScanAsyst mode under ambient conditions. All current-voltage measurements were performed in inert atmosphere using an Agilent 4156C semiconductor parameter analyzer. The effective device capacitances were obtained with an impedance analyzer (Solatron Analytical ModuLab XM MTS) with the transistors operated as plate capacitors (source and drain electrodes shorted and grounded) at a frequency of 100 Hz. Temperature-dependent electrical measurements were performed in vacuum ($< 10^{-6}$ mbar) in a cryogenic probe station with a closed cooling cycle (CRX-6.5 K, Lake Shore Cryotronics Inc.). Starting from the lowest temperature, the temperature was increased in steps of 25 K. Before each measurement, a hold time of 20 min ensured thermal equilibration.

Optical Measurements. PL spectra of SWCNT dispersions and network devices were acquired on a home-built laser setup. For excitation, the wavelength-filtered output of a picosecond-pulsed supercontinuum laser (Fianium Ltd. WhiteLase SC400, 20 MHz repetition rate) or the beam of a 785 nm laser diode (Alphalas GmbH, operated in continuous wave mode) were focused on the samples with a nIR-optimized 50 \times objective (Olympus, N.A. 0.65). Scattered laser light was blocked by appropriate longpass filters. Spectra were recorded with an Acton SpectraPro SP2358 spectrometer (grating blaze 1200 nm, 150 lines mm $^{-1}$) and a liquid nitrogen-cooled InGaAs line camera (Princeton Instruments OMA V:1024). For the acquisition of voltage-dependent PL and EL spectra, SWCNT network transistors were electrically connected and voltages were applied with a Keithley 2612A source meter. All spectra were corrected to account for the absorption of the optics in the detection path and wavelength-dependent detection efficiency. EL images of the transistor channels were recorded with a nIR-optimized 50 \times objective (Olympus, N.A. 0.65) and a thermoelectrically cooled InGaAs camera (Xenics XEVA-CL-TE3) during constant current sweeps (Keysight B1500A semiconductor parameter analyzer) of the devices. Total

electroluminescence intensities during constant current sweeps were measured with a calibrated InGaAs photodiode (Thorlabs FGA-21) and external efficiencies were calculated as reported previously,⁶⁹ taking into account the EL spectra and wavelength-dependent photodiode sensitivity.

Charge Modulation Photoluminescence (CMPL) Spectroscopy. CMPL spectroscopy was performed as previously described.⁵⁴ In brief, SWCNT network transistors were mounted on the laser setup as detailed above. The source and drain electrodes were grounded and the gate bias was modulated with a peak-to-peak voltage V_{pp} around an offset voltage V_{os} using a Keysight 33600A waveform generator, and SWCNT networks were simultaneously excited with a 785 nm laser diode (Alphas GmbH) operated in continuous wave mode. The spectrally resolved emission was detected with an InGaAs photodiode (Thorlabs FGA10) and the signal was pre-amplified (Femto DLPCA-200 transimpedance amplifier) and sent to a lock-in amplifier (Stanford Research Systems SR830) that was phase-locked to the waveform generator signal. The differential photoluminescence signal ΔPL was obtained after correction of the spectra to account for the absorption of optics in the detection path and the wavelength-dependent detection efficiency.

ASSOCIATED CONTENT

Supporting Information

Raman and absorption spectra of pristine and sp^3 -functionalized SWCNT dispersions, AFM image of a pristine SWCNT network, additional electrical characterization (transfer and output curves, linear mobilities, frequency-dependent capacitance) of pristine and sp^3 -functionalized SWCNT network FETs, EL spectra, voltage- and power-dependent PL spectra, estimation of excitation densities in EL and PL measurements, schematic setup for CMPL spectroscopy, additional voltage- and frequency-dependent CMPL spectra, calculation of trap densities from subthreshold swings, schematic device layout and details for gated four-point probe measurements, temperature-dependent carrier mobilities. **PDF**

AUTHOR INFORMATION

Corresponding Author

*E-mail: zaumseil@uni-heidelberg.de

ORCID

Nicolas F. Zorn: 0000-0001-9651-5612

Felix J. Berger: 0000-0003-2834-0050

Jana Zaumseil: 0000-0002-2048-217X

Notes

The authors declare no competing financial interest.

ACKNOWLEDGMENTS

This project has received funding from the European Research Council (ERC) under the European Union's Horizon 2020 research and innovation programme (Grant agreement no. 817494 "TRIFECTs").

REFERENCES

1. Avouris, P.; Freitag, M.; Perebeinos, V. Carbon-Nanotube Photonics and Optoelectronics. *Nat. Photonics* **2008**, *2*, 341–350.
2. Graf, A.; Held, M.; Zakharko, Y.; Tropf, L.; Gather, M. C.; Zaumseil, J. Electrical Pumping and Tuning of Exciton-Polaritons in Carbon Nanotube Microcavities. *Nat. Mater.* **2017**, *16*, 911-917.
3. Graf, A.; Murawski, C.; Zakharko, Y.; Zaumseil, J.; Gather, M. C. Infrared Organic Light-Emitting Diodes with Carbon Nanotube Emitters. *Adv. Mater.* **2018**, *30*, 1706711.
4. Liang, S.; Wei, N.; Ma, Z.; Wang, F.; Liu, H.; Wang, S.; Peng, L.-M. Microcavity-Controlled Chirality-Sorted Carbon Nanotube Film Infrared Light Emitters. *ACS Photonics* **2017**, *4*, 435–442.
5. Nish, A.; Hwang, J.-Y.; Doig, J.; Nicholas, R. J. Highly Selective Dispersion of Single-Walled Carbon Nanotubes Using Aromatic Polymers. *Nat. Nanotechnol.* **2007**, *2*, 640–646.
6. Gomulya, W.; Costanzo, G. D.; Carvalho, E. J. F. d.; Bisri, S. Z.; Derenskyi, V.; Fritsch, M.; Fröhlich, N.; Allard, S.; Gordiichuk, P.; Herrmann, A.; Marrink, S. J.; dos Santos, M. C.; Scherf, U.; Loi, M. A. Semiconducting Single-Walled Carbon Nanotubes on Demand by Polymer Wrapping. *Adv. Mater.* **2013**, *25*, 2948–2956.
7. Graf, A.; Zakharko, Y.; Schießl, S. P.; Backes, C.; Pfohl, M.; Flavel, B. S.; Zaumseil, J. Large Scale, Selective Dispersion of Long Single-Walled Carbon Nanotubes with High Photoluminescence Quantum Yield by Shear Force Mixing. *Carbon* **2016**, *105*, 593–599.

8. Rother, M.; Brohmann, M.; Yang, S.; Grimm, S. B.; Schießl, S. P.; Graf, A.; Zaumseil, J. Aerosol-Jet Printing of Polymer-Sorted (6,5) Carbon Nanotubes for Field-Effect Transistors with High Reproducibility. *Adv. Electron. Mater.* **2017**, *3*, 1700080.
9. Bucella, S. G.; Salazar-Rios, J. M.; Derenskyi, V.; Fritsch, M.; Scherf, U.; Loi, M. A.; Caironi, M. Inkjet Printed Single-Walled Carbon Nanotube Based Ambipolar and Unipolar Transistors for High-Performance Complementary Logic Circuits. *Adv. Electron. Mater.* **2016**, *2*, 1600094.
10. Schiessl, S. P.; Fröhlich, N.; Held, M.; Gannott, F.; Schweiger, M.; Forster, M.; Scherf, U.; Zaumseil, J. Polymer-Sorted Semiconducting Carbon Nanotube Networks for High-Performance Ambipolar Field-Effect Transistors. *ACS Appl. Mater. Interfaces* **2015**, *7*, 682–689.
11. Sun, J.; Sapkota, A.; Park, H.; Wesley, P.; Jung, Y.; Maskey, B. B.; Kim, Y.; Majima, Y.; Ding, J.; Ouyang, J.; Guo, C.; Lefebvre, J.; Li, Z.; Malenfant, P. R. L.; Javey, A.; Cho, G. Fully R2R-Printed Carbon-Nanotube-Based Limitless Length of Flexible Active-Matrix for Electrophoretic Display Application. *Adv. Electron. Mater.* **2020**, *6*, 1901431.
12. Hertel, T.; Himmelein, S.; Ackermann, T.; Stich, D.; Crochet, J. Diffusion Limited Photoluminescence Quantum Yields in 1-D Semiconductors: Single-Wall Carbon Nanotubes. *ACS Nano* **2010**, *4*, 7161–7168.
13. Perebeinos, V.; Tersoff, J.; Avouris, P. Scaling of Excitons in Carbon Nanotubes. *Phys. Rev. Lett.* **2004**, *92*, 257402.

14. Steiner, M.; Freitag, M.; Perebeinos, V.; Naumov, A.; Small, J. P.; Bol, A. A.; Avouris, P. Gate-Variable Light Absorption and Emission in a Semiconducting Carbon Nanotube. *Nano Lett.* **2009**, *9*, 3477-3481.
15. Rother, M.; Schießl, S. P.; Zakharko, Y.; Gannott, F.; Zaumseil, J. Understanding Charge Transport in Mixed Networks of Semiconducting Carbon Nanotubes. *ACS Appl. Mater. Interfaces* **2016**, *8*, 5571–5579.
16. Jakubka, F.; Backes, C.; Gannott, F.; Mundloch, U.; Hauke, F.; Hirsch, A.; Zaumseil, J. Mapping Charge Transport by Electroluminescence in Chirality-Selected Carbon Nanotube Networks. *ACS Nano* **2013**, *7*, 7428–7435.
17. Wang, J.; Shea, M. J.; Flach, J. T.; McDonough, T. J.; Way, A. J.; Zanni, M. T.; Arnold, M. S. Role of Defects as Exciton Quenching Sites in Carbon Nanotube Photovoltaics. *J. Phys. Chem. C* **2017**, *121*, 8310-8318.
18. Shiraki, T.; Miyauchi, Y.; Matsuda, K.; Nakashima, N. Carbon Nanotube Photoluminescence Modulation by Local Chemical and Supramolecular Chemical Functionalization. *Acc. Chem. Res.* **2020**, *53*, 1846-1859.
19. Brozena, A. H.; Kim, M.; Powell, L. R.; Wang, Y. Controlling the Optical Properties of Carbon Nanotubes with Organic Colour-Centre Quantum Defects. *Nat. Rev. Chem.* **2019**, *3*, 375-392.
20. Gifford, B. J.; Kilina, S.; Htoon, H.; Doorn, S. K.; Tretiak, S. Controlling Defect-State Photophysics in Covalently Functionalized Single-Walled Carbon Nanotubes. *Acc. Chem. Res.* **2020**, *53*, 1791-1801.

21. Ghosh, S.; Bachilo, S. M.; Simonette, R. A.; Beckingham, K. M.; Weisman, R. B. Oxygen Doping Modifies Near-Infrared Band Gaps in Fluorescent Single-Walled Carbon Nanotubes. *Science* **2010**, *330*, 1656-1659.
22. Kwon, H.; Furmanchuk, A.; Kim, M.; Meany, B.; Guo, Y.; Schatz, G. C.; Wang, Y. Molecularly Tunable Fluorescent Quantum Defects. *J. Am. Chem. Soc.* **2016**, *138*, 6878-6885.
23. Piao, Y.; Meany, B.; Powell, L. R.; Valley, N.; Kwon, H.; Schatz, G. C.; Wang, Y. Brightening of Carbon Nanotube Photoluminescence through the Incorporation of sp^3 Defects. *Nat. Chem.* **2013**, *5*, 840-845.
24. He, X.; Gifford, B. J.; Hartmann, N. F.; Ihly, R.; Ma, X.; Kilina, S. V.; Luo, Y.; Shayan, K.; Strauf, S.; Blackburn, J. L.; Tretiak, S.; Doorn, S. K.; Htoon, H. Low-Temperature Single Carbon Nanotube Spectroscopy of sp^3 Quantum Defects. *ACS Nano* **2017**, *11*, 10785-10796.
25. Settele, S.; Berger, F. J.; Lindenthal, S.; Zhao, S.; El Yumin, A. A.; Zorn, N. F.; Asyuda, A.; Zharnikov, M.; Högele, A.; Zaumseil, J. Synthetic Control over the Binding Configuration of Luminescent sp^3 -Defects in Single-Walled Carbon Nanotubes. *Nat. Commun.* **2021**, *12*, 2119.
26. Hartmann, N. F.; Velizhanin, K. A.; Haroz, E. H.; Kim, M.; Ma, X.; Wang, Y.; Htoon, H.; Doorn, S. K. Photoluminescence Dynamics of Aryl sp^3 Defect States in Single-Walled Carbon Nanotubes. *ACS Nano* **2016**, *10*, 8355-8365.
27. Ma, X.; Hartmann, N. F.; Baldwin, J. K. S.; Doorn, S. K.; Htoon, H. Room-Temperature Single-Photon Generation from Solitary Dopants of Carbon Nanotubes. *Nat. Nanotechnol.* **2015**, *10*, 671-675.

28. He, X.; Hartmann, N. F.; Ma, X.; Kim, Y.; Ihly, R.; Blackburn, J. L.; Gao, W.; Kono, J.; Yomogida, Y.; Hirano, A.; Tanaka, T.; Kataura, H.; Htoon, H.; Doorn, S. K. Tunable Room-Temperature Single-Photon Emission at Telecom Wavelengths from sp^3 Defects in Carbon Nanotubes. *Nat. Photonics* **2017**, *11*, 577.
29. Luo, Y.; He, X.; Kim, Y.; Blackburn, J. L.; Doorn, S. K.; Htoon, H.; Strauf, S. Carbon Nanotube Color Centers in Plasmonic Nanocavities: A Path to Photon Indistinguishability at Telecom Bands. *Nano Lett.* **2019**, *19*, 9037-9044.
30. Wilson, H.; Ripp, S.; Prisbrey, L.; Brown, M. A.; Sharf, T.; Myles, D. J. T.; Blank, K. G.; Minot, E. D. Electrical Monitoring of sp^3 Defect Formation in Individual Carbon Nanotubes. *J. Phys. Chem. C* **2016**, *120*, 1971-1976.
31. Lee, Y.-S.; Nardelli, M. B.; Marzari, N. Band Structure and Quantum Conductance of Nanostructures from Maximally Localized Wannier Functions: The Case of Functionalized Carbon Nanotubes. *Phys. Rev. Lett.* **2005**, *95*, 076804.
32. Bouilly, D.; Hon, J.; Daly, N. S.; Trocchia, S.; Vernick, S.; Yu, J.; Warren, S.; Wu, Y.; Gonzalez, R. L.; Shepard, K. L.; Nuckolls, C. Single-Molecule Reaction Chemistry in Patterned Nanowells. *Nano Lett.* **2016**, *16*, 4679-4685.
33. Lee, Y.; Trocchia, S. M.; Warren, S. B.; Young, E. F.; Vernick, S.; Shepard, K. L. Electrically Controllable Single-Point Covalent Functionalization of Spin-Cast Carbon-Nanotube Field-Effect Transistor Arrays. *ACS Nano* **2018**, *12*, 9922-9930.
34. Berger, F. J.; Lüttgens, J.; Nowack, T.; Kutsch, T.; Lindenthal, S.; Kistner, L.; Müller, C. C.; Bongartz, L. M.; Lumsargis, V. A.; Zakharko, Y.; Zaumseil, J. Brightening of Long, Polymer-

Wrapped Carbon Nanotubes by sp^3 Functionalization in Organic Solvents. *ACS Nano* **2019**, *13*, 9259-9269.

35. Saha, A.; Gifford, B. J.; He, X.; Ao, G.; Zheng, M.; Kataura, H.; Htoon, H.; Kilina, S.; Tretiak, S.; Doorn, S. K. Narrow-Band Single-Photon Emission through Selective Aryl Functionalization of Zigzag Carbon Nanotubes. *Nat. Chem.* **2018**, *10*, 1089-1095.

36. Gifford, B. J.; Kilina, S.; Htoon, H.; Doorn, S. K.; Tretiak, S. Exciton Localization and Optical Emission in Aryl-Functionalized Carbon Nanotubes. *J. Phys. Chem. C* **2018**, *122*, 1828-1838.

37. Schirowski, M.; Hauke, F.; Hirsch, A. Controlling the Degree of Functionalization: In-Depth Quantification and Side-Product Analysis of Diazonium Chemistry on SWCNTs. *Chem. Eur. J.* **2019**, *25*, 12761-12768.

38. Qian, Q.; Li, G.; Jin, Y.; Liu, J.; Zou, Y.; Jiang, K.; Fan, S.; Li, Q. Trap-State-Dominated Suppression of Electron Conduction in Carbon Nanotube Thin-Film Transistors. *ACS Nano* **2014**, *8*, 9597-9605.

39. Schießl, S. P.; Rother, M.; Lüttgens, J.; Zaumseil, J. Extracting the Field-Effect Mobilities of Random Semiconducting Single-Walled Carbon Nanotube Networks: A Critical Comparison of Methods. *Appl. Phys. Lett.* **2017**, *111*, 193301.

40. Zaumseil, J. Recent Developments and Novel Applications of Thin Film, Light-Emitting Transistors. *Adv. Funct. Mater.* **2020**, *30*, 1905269.

41. Brohmann, M.; Wieland, S.; Angstenberger, S.; Herrmann, N. J.; Lüttgens, J.; Fazzi, D.; Zaumseil, J. Guiding Charge Transport in Semiconducting Carbon Nanotube Networks by Local Optical Switching. *ACS Appl. Mater. Interfaces* **2020**, *12*, 28392-28403.
42. Zaumseil, J.; Kline, R. J.; Sirringhaus, H. Electroluminescence Imaging and Microstructure of Organic Light-Emitting Field-Effect Transistors. *Appl. Phys. Lett.* **2008**, *92*, 073304.
43. Kadria-Vili, Y.; Bachilo, S. M.; Blackburn, J. L.; Weisman, R. B. Photoluminescence Side Band Spectroscopy of Individual Single-Walled Carbon Nanotubes. *J. Phys. Chem. C* **2016**, *120*, 23898-23904.
44. Lüttgens, J. M.; Berger, F. J.; Zaumseil, J. Population of Exciton–Polaritons via Luminescent sp^3 Defects in Single-Walled Carbon Nanotubes. *ACS Photonics* **2020**, *8*, 182-193.
45. Jakubka, F.; Grimm, S. B.; Zakharko, Y.; Gannott, F.; Zaumseil, J. Trion Electroluminescence from Semiconducting Carbon Nanotubes. *ACS Nano* **2014**, *8*, 8477–8486.
46. Iwamura, M.; Akizuki, N.; Miyauchi, Y.; Mouri, S.; Shaver, J.; Gao, Z.; Cagnet, L.; Lounis, B.; Matsuda, K. Nonlinear Photoluminescence Spectroscopy of Carbon Nanotubes with Localized Exciton States. *ACS Nano* **2014**, *8*, 11254-11260.
47. Mehlenbacher, R. D.; McDonough, T. J.; Grechko, M.; Wu, M.-Y.; Arnold, M. S.; Zanni, M. T. Energy Transfer Pathways in Semiconducting Carbon Nanotubes Revealed Using Two-Dimensional White-Light Spectroscopy. *Nat. Commun.* **2015**, *6*, 321.

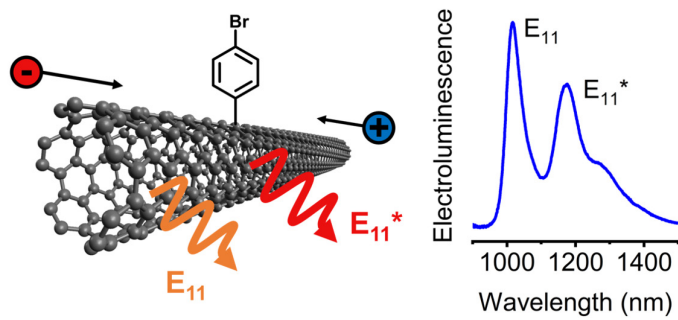
48. Xu, B.; Wu, X.; Kim, M.; Wang, P.; Wang, Y. Electroluminescence from 4-Nitroaryl Organic Color Centers in Semiconducting Single-Wall Carbon Nanotubes. *J. Appl. Phys.* **2021**, *129*, 044305.
49. Kinder, J. M.; Mele, E. J. Nonradiative Recombination of Excitons in Carbon Nanotubes Mediated by Free Charge Carriers. *Phys. Rev. B* **2008**, *78*, 155429.
50. Shiraishi, T.; Shiraki, T.; Nakashima, N. Substituent Effects on the Redox States of Locally Functionalized Single-Walled Carbon Nanotubes Revealed by *in Situ* Photoluminescence Spectroelectrochemistry. *Nanoscale* **2017**, *9*, 16900-16907.
51. Shiraishi, T.; Juhász, G.; Shiraki, T.; Akizuki, N.; Miyauchi, Y.; Matsuda, K.; Nakashima, N. Determination of Precise Redox Properties of Oxygen-Doped Single-Walled Carbon Nanotubes Based on *in Situ* Photoluminescence Electrochemistry. *J. Phys. Chem. C* **2016**, *120*, 15632-15639.
52. Caironi, M.; Bird, M.; Fazzi, D.; Chen, Z.; Di Pietro, R.; Newman, C.; Facchetti, A.; Sirringhaus, H. Very Low Degree of Energetic Disorder as the Origin of High Mobility in an *n*-Channel Polymer Semiconductor. *Adv. Funct. Mater.* **2011**, *21*, 3371–3381.
53. Meneau, A. Y. B.; Olivier, Y.; Backlund, T.; James, M.; Breiby, D. W.; Andreasen, J. W.; Sirringhaus, H. Temperature Dependence of Charge Localization in High-Mobility, Solution-Crystallized Small Molecule Semiconductors Studied by Charge Modulation Spectroscopy. *Adv. Funct. Mater.* **2016**, *26*, 2326-2333.

54. Zorn, N. F.; Scuratti, F.; Berger, F. J.; Perinot, A.; Heimfarth, D.; Caironi, M.; Zaumseil, J. Probing Mobile Charge Carriers in Semiconducting Carbon Nanotube Networks by Charge Modulation Spectroscopy. *ACS Nano* **2020**, *14*, 2412-2423.
55. He, X.; Velizhanin, K. A.; Bullard, G.; Bai, Y.; Olivier, J.-H.; Hartmann, N. F.; Gifford, B. J.; Kilina, S.; Tretiak, S.; Htoon, H.; Therien, M. J.; Doorn, S. K. Solvent- and Wavelength-Dependent Photoluminescence Relaxation Dynamics of Carbon Nanotube sp^3 Defect States. *ACS Nano* **2018**, *12*, 8060-8070.
56. Sakanoue, T.; Sirringhaus, H. Band-Like Temperature Dependence of Mobility in a Solution-Processed Organic Semiconductor. *Nat. Mater.* **2010**, *9*, 736-740.
57. Kalb, W. L.; Batlogg, B. Calculating the Trap Density of States in Organic Field-Effect Transistors from Experiment: A Comparison of Different Methods. *Phys. Rev. B* **2010**, *81*, 035327.
58. Gotthardt, J. M.; Schneider, S.; Brohmann, M.; Leingang, S.; Sauter, E.; Zharnikov, M.; Himmel, H.-J.; Zaumseil, J. Molecular n -Doping of Large- and Small-Diameter Carbon Nanotube Field-Effect Transistors with Tetrakis(tetramethylguanidino)benzene. *ACS Appl. Electron. Mater.* **2021**, *3*, 804-812.
59. Lee, S.-H.; Xu, Y.; Khim, D.; Park, W.-T.; Kim, D.-Y.; Noh, Y.-Y. Effect of Polymer Gate Dielectrics on Charge Transport in Carbon Nanotube Network Transistors: Low-K Insulator for Favorable Active Interface. *ACS Appl. Mater. Interfaces* **2016**, *8*, 32421-32431.
60. Itkis, M. E.; Pekker, A.; Tian, X.; Bekyarova, E.; Haddon, R. C. Networks of Semiconducting SWNTs: Contribution of Midgap Electronic States to the Electrical Transport. *Acc. Chem. Res.* **2015**, *48*, 2270-2279.

61. Brohmann, M.; Rother, M.; Schießl, S. P.; Preis, E.; Allard, S.; Scherf, U.; Zaumseil, J. Temperature-Dependent Charge Transport in Polymer-Sorted Semiconducting Carbon Nanotube Networks with Different Diameter Distributions. *J. Phys. Chem. C* **2018**, *122*, 19886–19896.
62. Choi, H. H.; Rodionov, Y. I.; Paterson, A. F.; Panidi, J.; Saranin, D.; Kharlamov, N.; Didenko, S. I.; Anthopoulos, T. D.; Cho, K.; Podzorov, V. Accurate Extraction of Charge Carrier Mobility in 4-Probe Field-Effect Transistors. *Adv. Funct. Mater.* **2018**, *28*, 1707105.
63. Brohmann, M.; Berger, F. J.; Matthiesen, M.; Schießl, S. P.; Schneider, S.; Zaumseil, J. Charge Transport in Mixed Semiconducting Carbon Nanotube Networks with Tailored Mixing Ratios. *ACS Nano* **2019**, *13*, 7323-7332.
64. Tessler, N.; Preezant, Y.; Rappaport, N.; Roichman, Y. Charge Transport in Disordered Organic Materials and Its Relevance to Thin-Film Devices: A Tutorial Review. *Adv. Mater.* **2009**, *21*, 2741-2761.
65. Statz, M.; Schneider, S.; Berger, F. J.; Lai, L.; Wood, W. A.; Abdi-Jalebi, M.; Leingang, S.; Himmel, H.-J.; Zaumseil, J.; Siringhaus, H. Charge and Thermoelectric Transport in Polymer-Sorted Semiconducting Single-Walled Carbon Nanotube Networks. *ACS Nano* **2020**, *14*, 15552-15565.
66. Zhou, X.; Park, J.-Y.; Huang, S.; Liu, J.; McEuen, P. L. Band Structure, Phonon Scattering, and the Performance Limit of Single-Walled Carbon Nanotube Transistors. *Phys. Rev. Lett.* **2005**, *95*, 146805.

67. Ferguson, A. J.; Reid, O. G.; Nanayakkara, S. U.; Ihly, R.; Blackburn, J. L. Efficiency of Charge-Transfer Doping in Organic Semiconductors Probed with Quantitative Microwave and Direct-Current Conductance. *J. Phys. Chem. Lett.* **2018**, *9*, 6864–6870.
68. Jensen, S. A.; Ulbricht, R.; Narita, A.; Feng, X.; Müllen, K.; Hertel, T.; Turchinovich, D.; Bonn, M. Ultrafast Photoconductivity of Graphene Nanoribbons and Carbon Nanotubes. *Nano Lett.* **2013**, *13*, 5925-5930.
69. Held, M.; Zakharko, Y.; Wang, M.; Jakubka, F.; Gannott, F.; Rumer, J. W.; Ashraf, R. S.; McCulloch, I.; Zaumseil, J. Photo- and Electroluminescence of Ambipolar, High-Mobility, Donor-Acceptor Polymers. *Org. Electron.* **2016**, *32*, 220-227.

FOR TABLE OF CONTENTS ONLY



Supporting Information

Charge Transport in and Electroluminescence from sp^3 -Functionalized Carbon Nanotube Networks

*Nicolas F. Zorn, Felix J. Berger, and Jana Zaumseil**

Institute for Physical Chemistry and Centre for Advanced Materials, Universität Heidelberg,
D-69120 Heidelberg, Germany

Corresponding Author

*E-mail: zaumseil@uni-heidelberg.de

Raman and Absorption Spectroscopy of (6,5) SWCNTs.....	S-3
Raman and Absorption Spectroscopy of sp^3 -Functionalized (6,5) SWCNTs.....	S-4
Atomic Force Microscopy.....	S-5
Electrical Characterization of SWCNT FETs	S-6
Transfer Characteristics and Voltage-Dependent Linear Mobilities.....	S-6
Output Characteristics	S-7
Linear Mobilities <i>versus</i> Defect Metrics	S-8
Frequency-Dependent Capacitance Measurements.....	S-9
Spectroscopic Characterization of SWCNT FETs	S-10
Electroluminescence Spectroscopy	S-10
Voltage- and Excitation Power-Dependent Photoluminescence Spectroscopy	S-13
Estimation of Excitation Densities in EL and PL Spectroscopy of SWCNT Networks ...	S-18
Charge Modulation Photoluminescence Spectroscopy	S-20
Temperature-Dependent Electrical Characterization of SWCNT FETs	S-23
Extraction of Trap Densities from the Subthreshold Regime	S-23
Schematic Device Layout and Principle of Gated Four-Point Probe Measurements.....	S-24
Temperature-Dependent Mobilities	S-25
REFERENCES.....	S-26

Raman and Absorption Spectroscopy of (6,5) SWCNTs

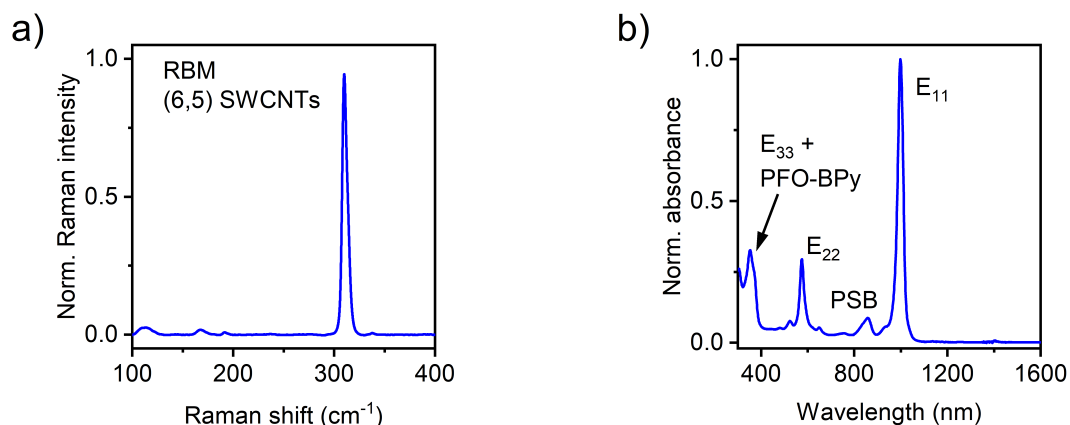


Figure S1. Characterization of PFO-BPy-wrapped (6,5) SWCNTs. **a)** Raman spectrum of a drop-cast film of (6,5) SWCNTs in the radial breathing mode (RBM) region. The absence of other peaks confirms the high purity of the dispersion without residual metallic nanotubes or other minority species. The excitation wavelength was 532 nm, and the data was baseline-corrected and averaged over 4000 spectra. **b)** UV-vis-nIR absorption spectrum of a (6,5) SWCNT dispersion in toluene. The main excitonic transitions (E_{11} , E_{22} , E_{33}), the E_{11} phonon side band (PSB), and the absorption band of the wrapping polymer are indicated. No other absorption peaks corresponding to larger-diameter chiralities are observed in the nIR region up to 1600 nm.

Raman and Absorption Spectroscopy of sp^3 -Functionalized (6,5) SWCNTs

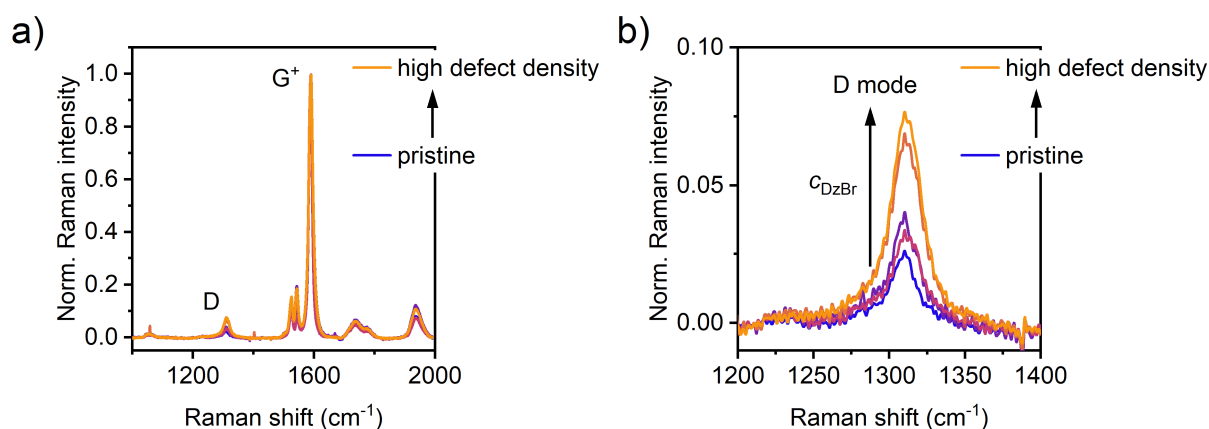


Figure S2. **a)** Raman spectra of drop-cast SWCNT films in the G-mode region and **b)** zoom-in on the D-mode. The increase in the D/G^+ area ratio is attributed to a higher density of introduced sp^3 defects for higher diazonium salt concentrations (C_{DzBr}). For all spectra, the excitation wavelength was 532 nm, and the data was baseline-corrected and averaged over 4000 spectra.

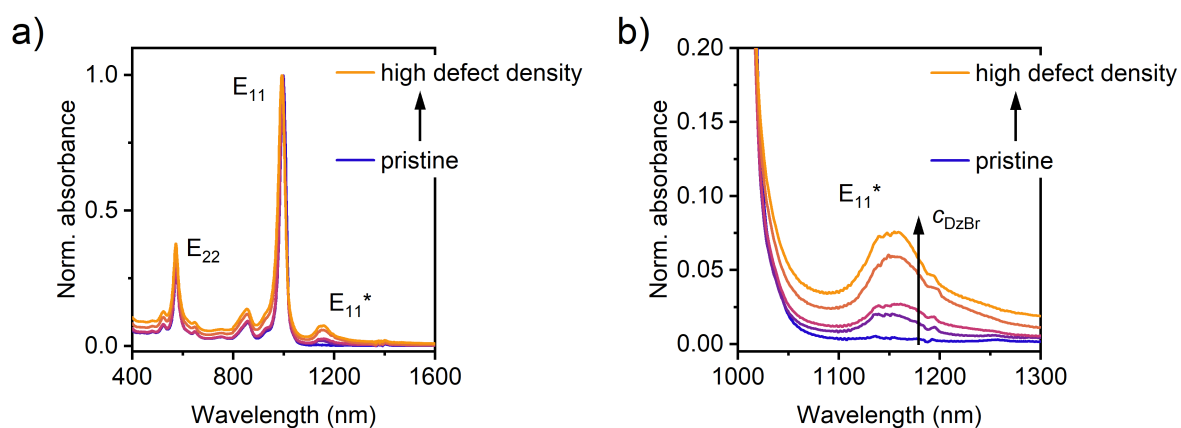


Figure S3. **a)** UV-vis-nIR absorption spectra of pristine and sp^3 -functionalized SWCNT dispersions. **b)** Zoom-in on the E_{11}^* defect state absorption band that increases with the diazonium salt concentration (C_{DzBr}).

Atomic Force Microscopy

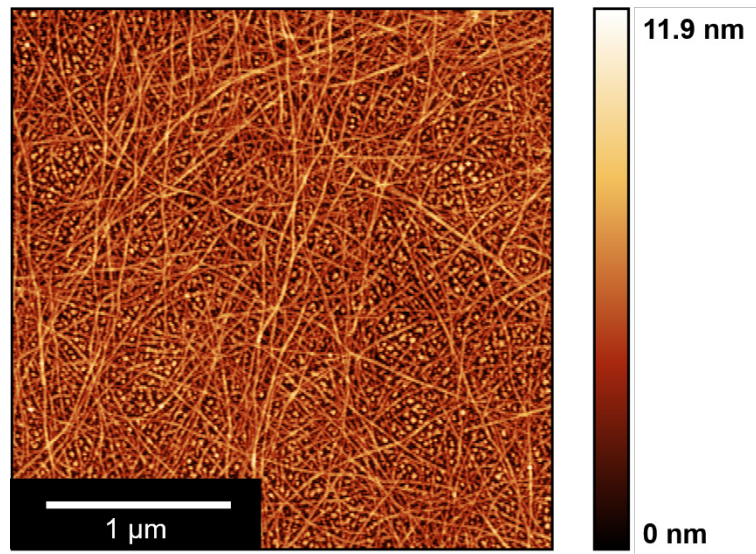


Figure S4. Atomic force micrograph of a dense, pristine SWCNT network used for the FET fabrication in this study. Scalebar is 1 μm.

Electrical Characterization of SWCNT FETs

Transfer Characteristics and Voltage-Dependent Linear Mobilities

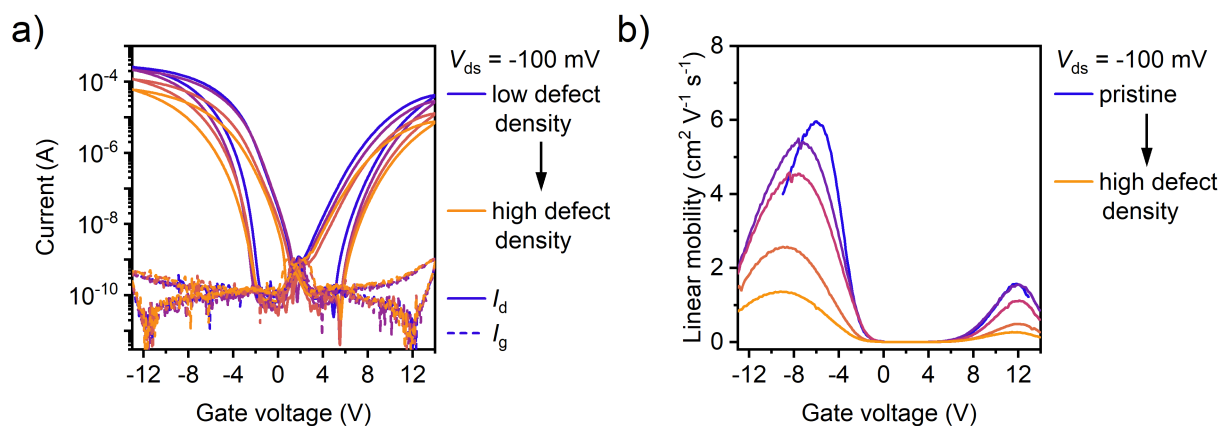


Figure S5. a) Representative transfer characteristics (source-drain voltage $V_{ds} = -100$ mV) of ambipolar FETs based on dense networks of sp^3 -functionalized (6,5) SWCNTs with different defect densities (drain currents I_d , solid lines; gate leakage currents I_g , dashed lines). **b)** Voltage-dependent linear charge carrier mobilities of pristine and sp^3 -functionalized SWCNT network FETs. Only forward sweeps are shown for clarity.

Output Characteristics

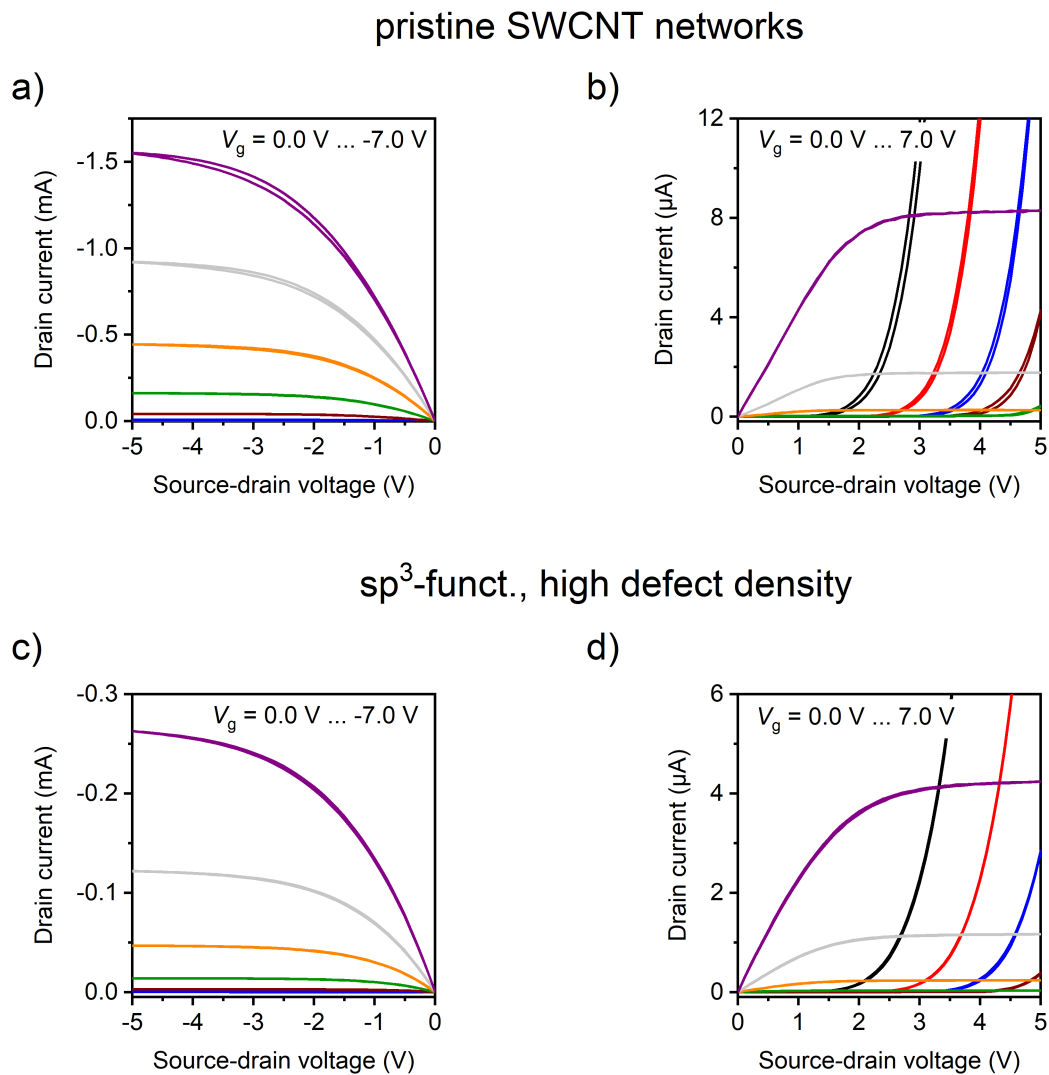


Figure S6. Representative output characteristics of ambipolar FETs based on dense networks of **a, b)** pristine SWCNTs and **c, d)** sp^3 -functionalized SWCNTs with a high defect density in hole and electron accumulation, respectively.

Linear Mobilities *versus* Defect Metrics

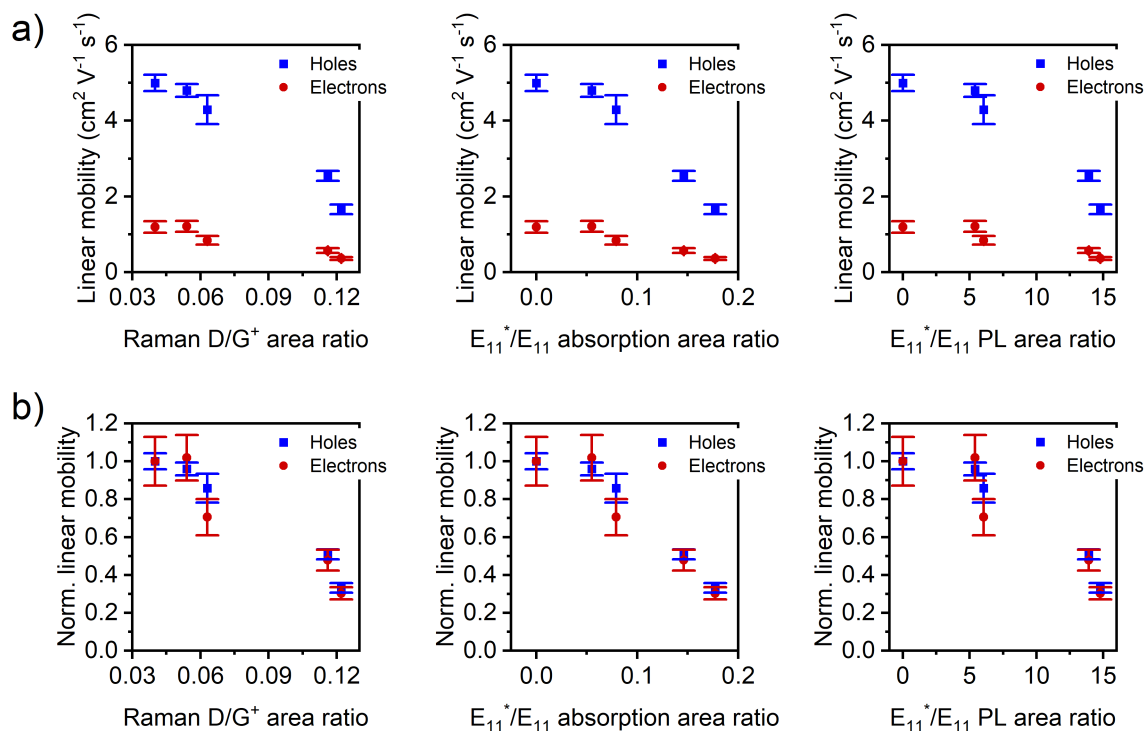


Figure S7. a) Absolute linear charge carrier mobilities (holes, blue squares; electrons, red circles) of pristine and sp^3 -functionalized (6,5) SWCNT network FETs *vs.* the Raman D/G⁺ area ratio, the E₁₁^{*}/E₁₁ absorption area ratio, and the E₁₁^{*}/E₁₁ PL area ratio, respectively. **b)** Linear charge carrier mobilities normalized to the pristine reference *vs.* defect metrics. Displayed values are maximum carrier mobilities and were averaged over several devices, error bars are standard deviations.

Frequency-Dependent Capacitance Measurements

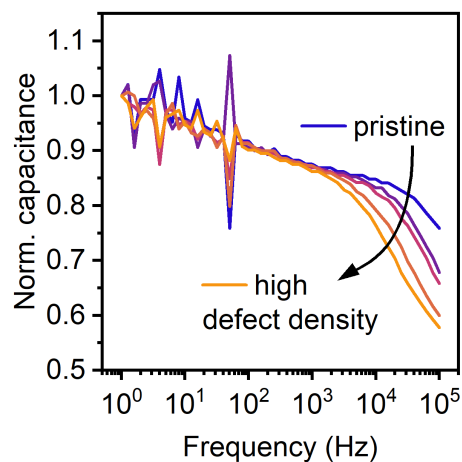


Figure S8. Normalized frequency-dependent capacitance of pristine and sp^3 -functionalized SWCNT network FETs measured in the on-state of the devices (gate voltage $V_g = -5$ V). The decrease in charge carrier mobilities results in a lower cut-off frequency of the transistors.

Table S1. Areal capacitances of pristine and sp^3 -functionalized SWCNT network FETs extracted in the on-state of the devices.

Sample	SWCNT network capacitance (nF/cm ²)
Pristine	110
Low defect density	118
Medium-low defect density	118
Medium-high defect density	118
High defect density	117

Spectroscopic Characterization of SWCNT FETs

Electroluminescence Spectroscopy

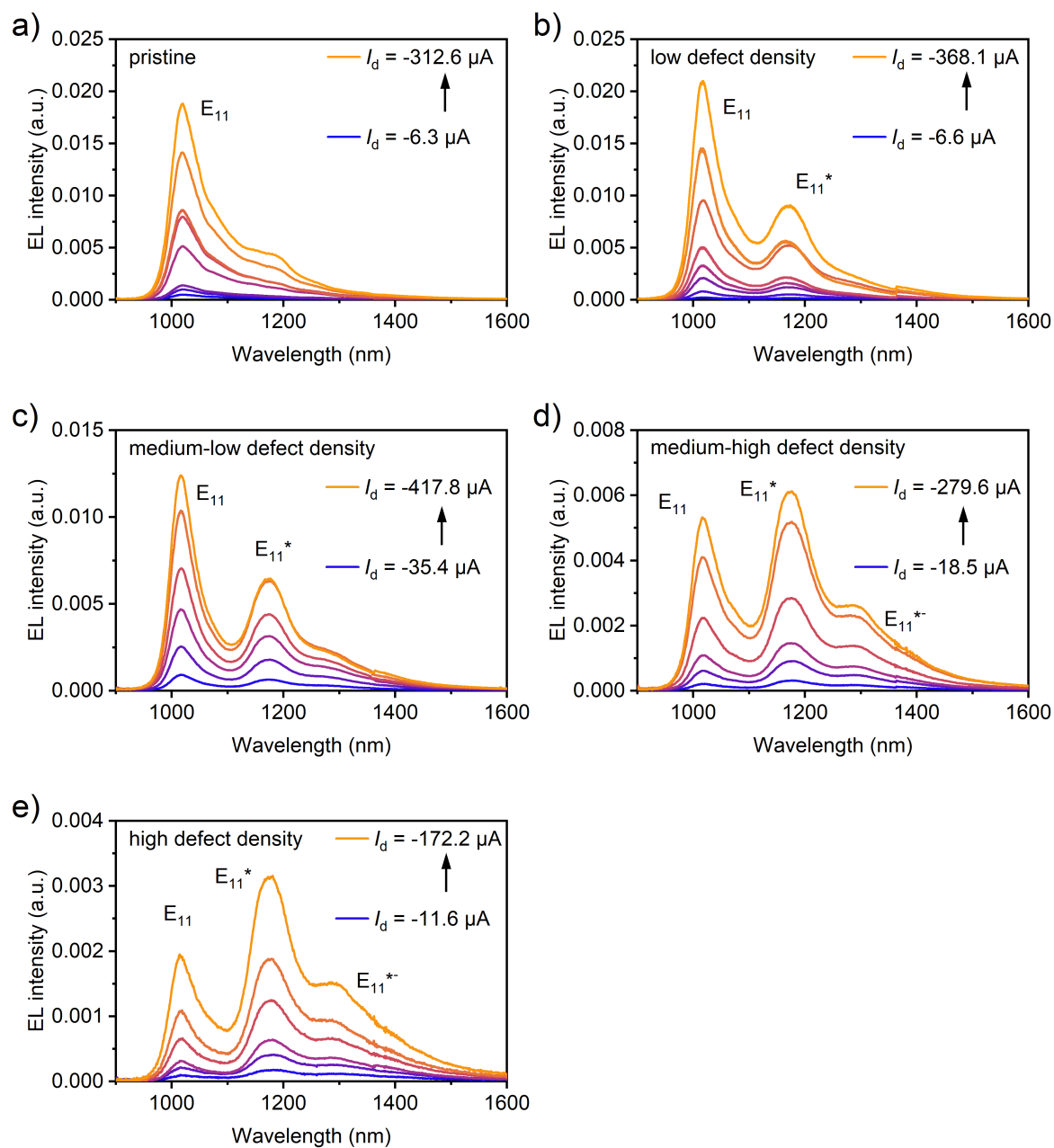


Figure S9. EL spectra of **a)** pristine and **b-e)** sp^3 -functionalized SWCNT network FETs with different defect densities for different drain currents (corresponding gate voltages vary from -2.2 V to -5.0 V). With increasing level of sp^3 functionalization, emission from the defect states becomes more dominant.

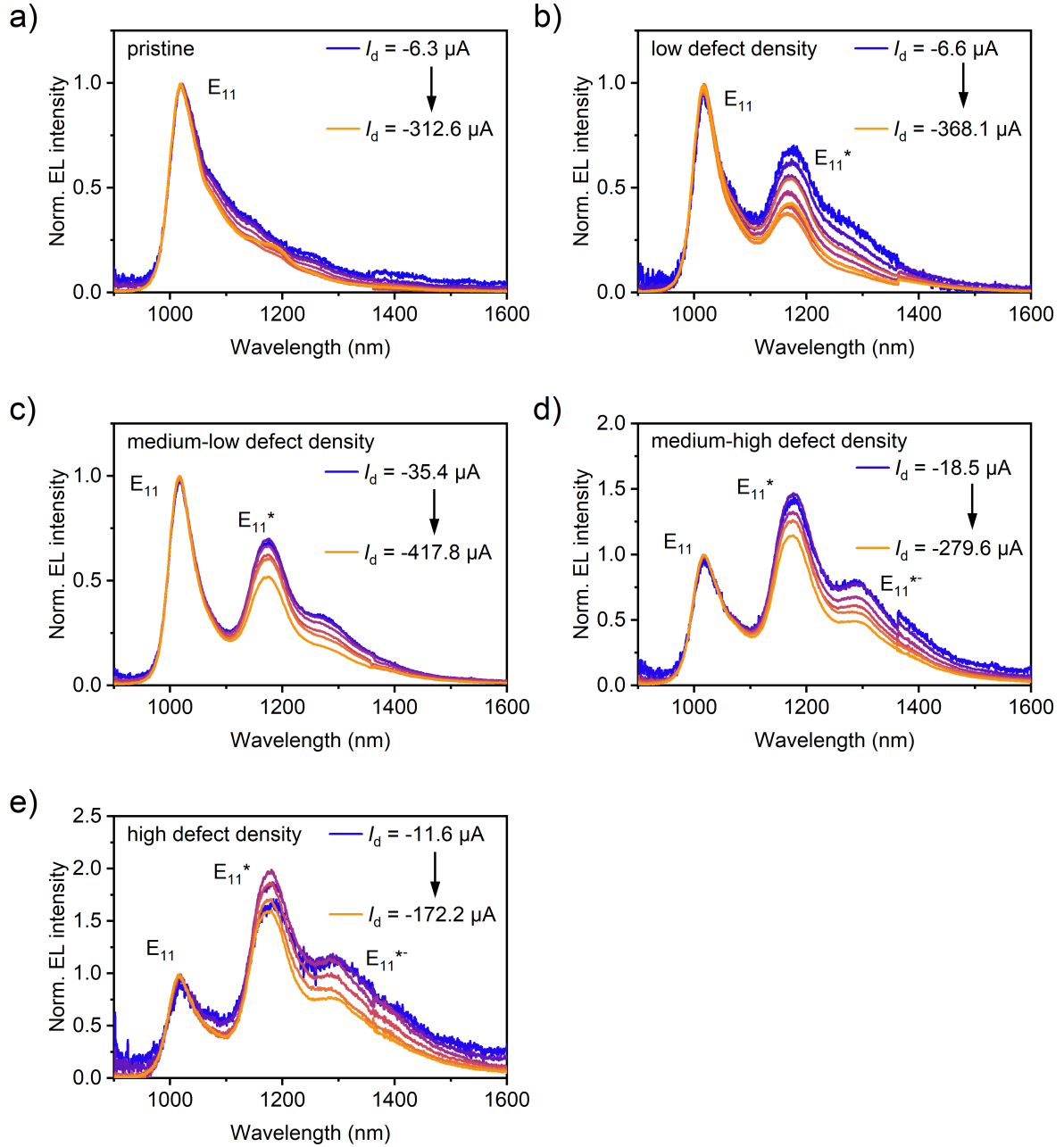


Figure S10. EL spectra normalized to the E_{11} exciton peak of **a)** pristine and **b-e)** sp^3 -functionalized SWCNT network FETs with different defect densities for different drain currents (corresponding gate voltages vary from -2.2 V to -5.0 V). sp^3 Defect emission is stable over one to two orders of magnitude in current density. Only a slight decrease of the defect-to- E_{11} emission ratio with increasing drain currents is observed.

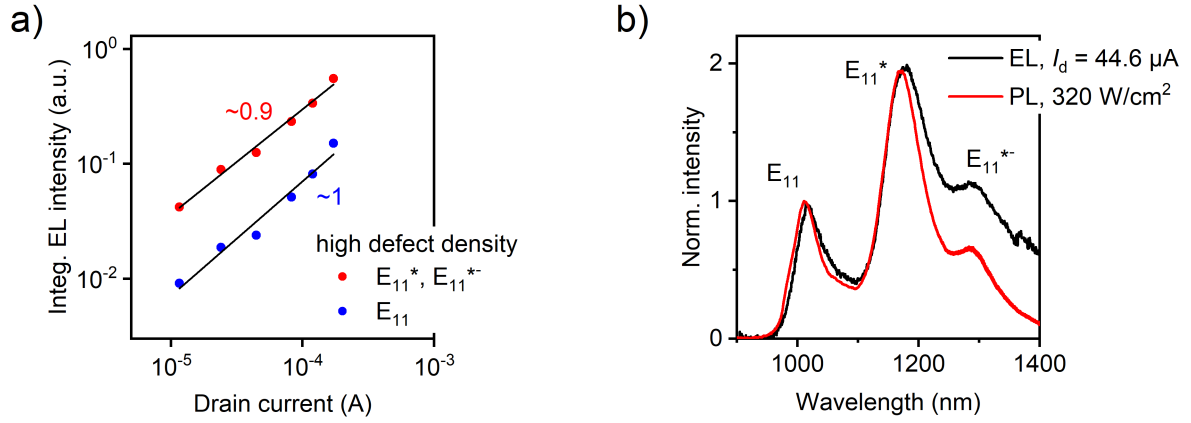


Figure S11. a) Log-log plot of the integrated EL intensity of a high defect density sp^3 -functionalized SWCNT network FET (corresponding spectra shown in **Figure 3e** of the main text) depending on the drain current. The slopes are ~ 1 , indicating that the experiments were conducted in the linear excitation regime where no state-filling is expected. **b)** Comparison between a normalized PL spectrum (low-power, non-resonant continuous wave excitation at 785 nm) and a normalized EL spectrum.

Voltage- and Excitation Power-Dependent Photoluminescence Spectroscopy

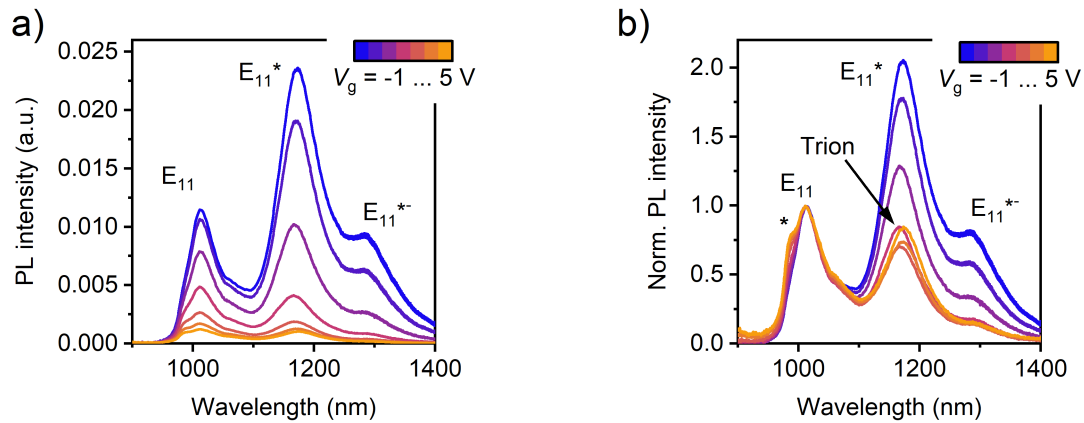


Figure S12. **a)** Static, gate voltage-dependent PL spectra (source-drain voltage $V_{ds} = -10$ mV) of an sp^3 -functionalized SWCNT network FET with high defect density in electron accumulation. **b)** Spectra normalized to the E_{11} exciton peak. At high voltages, PL from negatively charged trions can be observed at very similar wavelengths to the E_{11}^* emission. All spectra were acquired under non-resonant continuous wave excitation (785 nm, ~ 320 W cm^{-2}). Note that the peak at ~ 985 nm marked with an asterisk corresponds to the Raman 2D mode of (6,5) SWCNTs.

pristine SWCNT networks

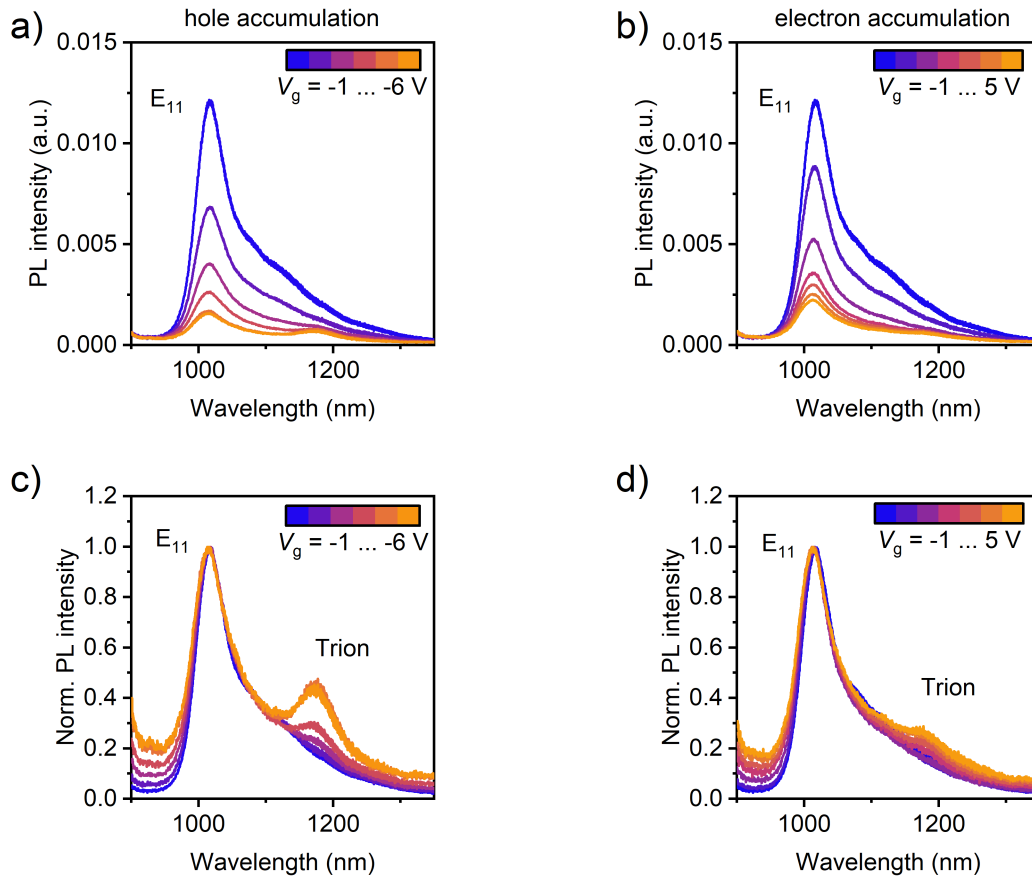


Figure S13. **a, b)** Static, gate voltage-dependent PL spectra (source-drain voltage $V_{ds} = -10$ mV) of a pristine (6,5) SWCNT network FET in hole and electron accumulation, respectively. **c, d)** Spectra normalized to the E_{11} exciton peak. At high voltages, PL from positively and negatively charged trions, respectively, can be observed. All spectra were acquired under pulsed excitation at the E_{22} transition (575 nm, ~ 0.02 mJ cm $^{-2}$).

sp³-funct., high defect density

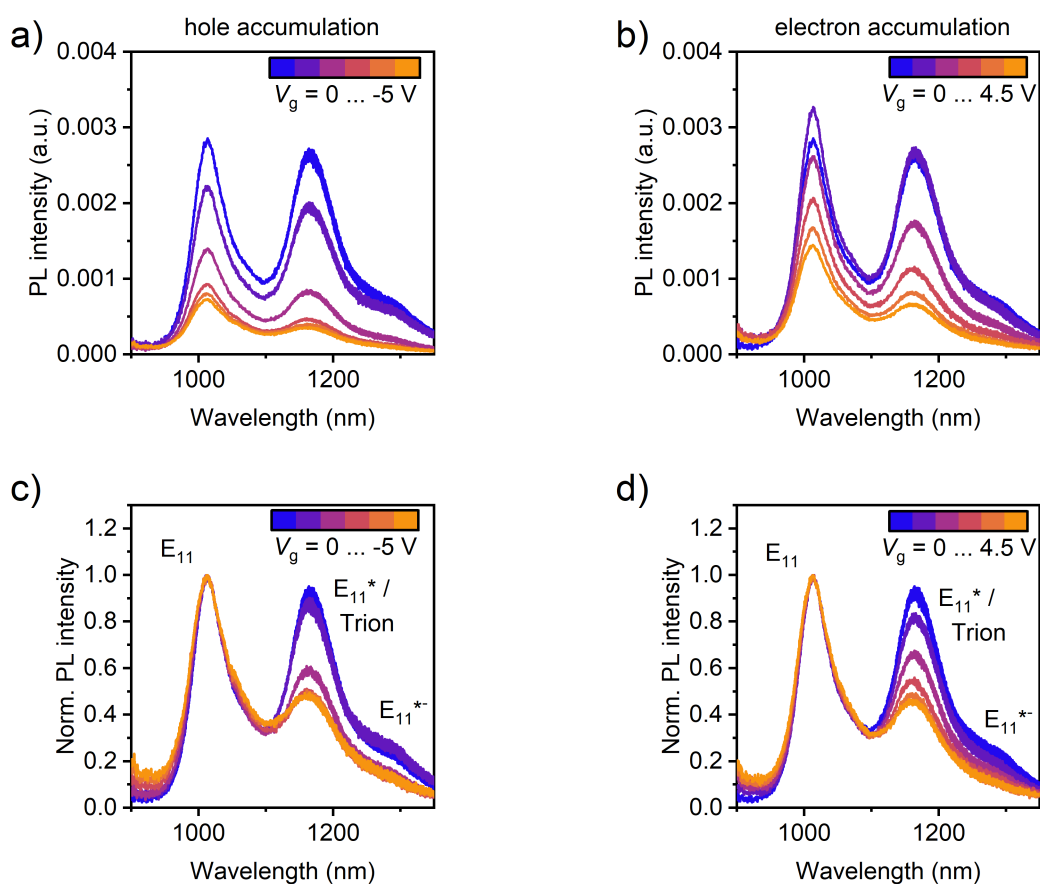


Figure S14. **a, b)** Static, gate voltage-dependent PL spectra (source-drain voltage $V_{ds} = -10$ mV) of an sp³-functionalized SWCNT network FET with high defect density in hole and electron accumulation, respectively. **c, d)** Spectra normalized to the E₁₁ exciton peak. At high voltages, PL from positively and negatively charged triions, respectively, can be observed at very similar wavelengths to the E₁₁* emission. All spectra were acquired under pulsed excitation at the E₂₂ transition (575 nm, ~ 0.02 mJ cm⁻²).

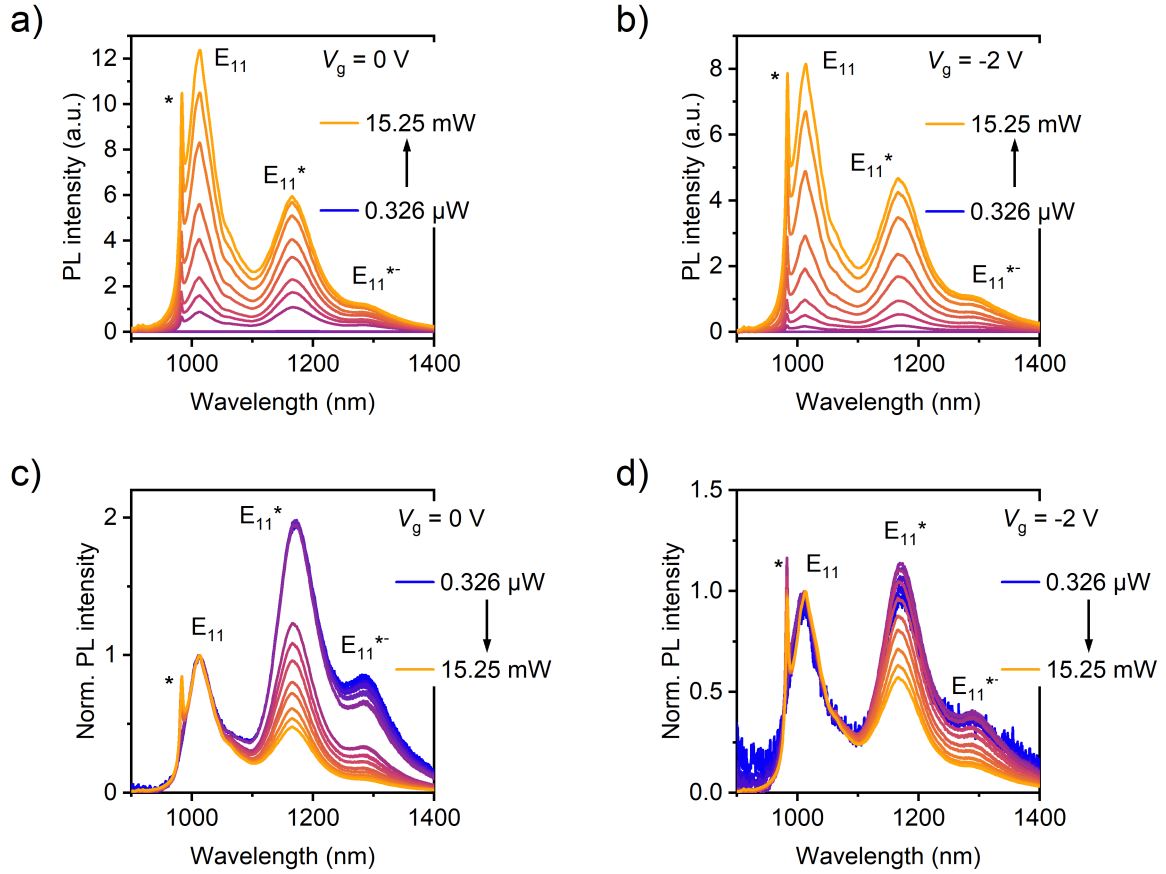


Figure S15. Excitation power-dependent PL spectra of an sp^3 -functionalized SWCNT network FET with high defect density **a)** without applied bias ($V_g = 0$ V) and **b)** at $V_g = -2$ V under continuous wave excitation (785 nm). **c, d)** Spectra normalized to the E_{11} exciton peak show saturation of E_{11}^* and E_{11}^{*-} emission at higher excitation densities. Note that the sharp peak at ~ 985 nm marked with an asterisk corresponds to the Raman 2D mode of (6,5) SWCNTs.

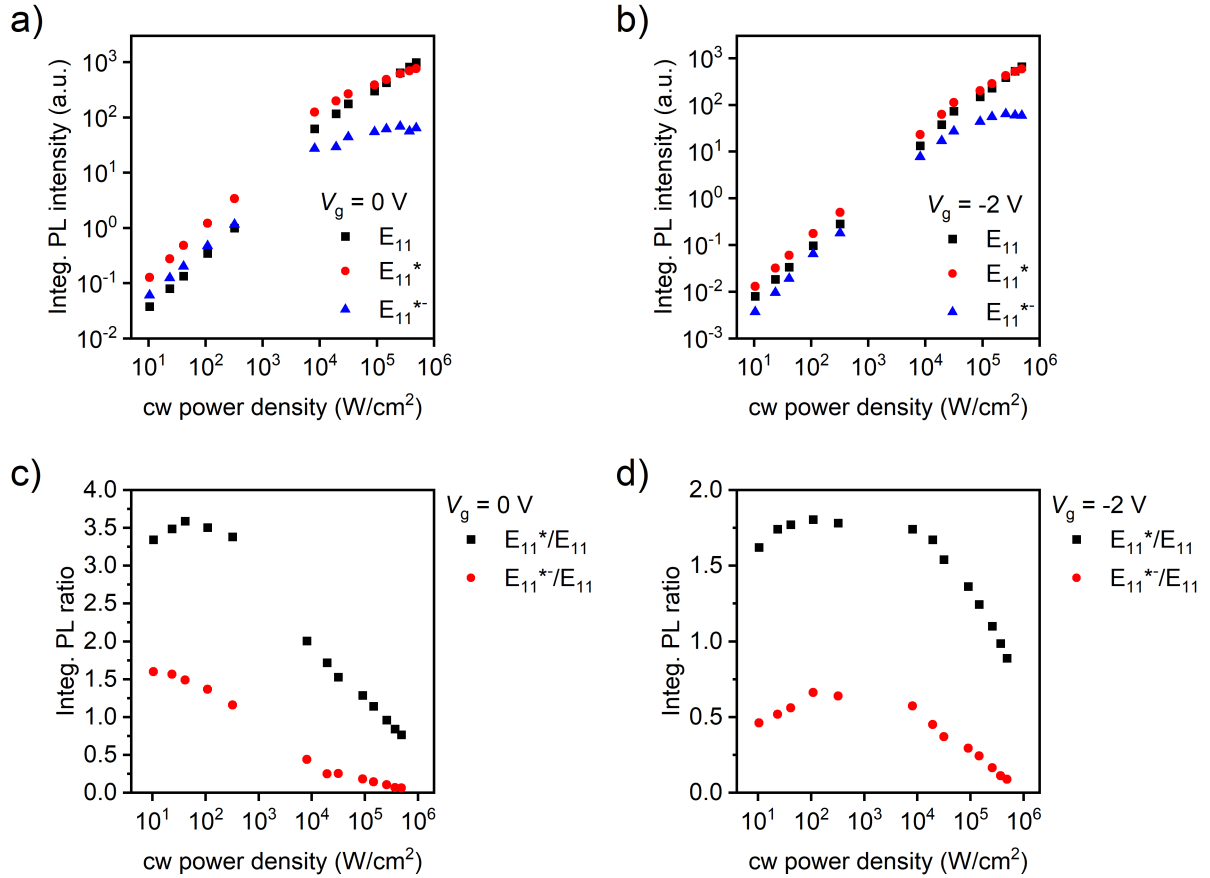


Figure S16. Excitation power-dependent, integrated PL intensities of an sp^3 -functionalized SWCNT network FET with high defect density **a)** without applied bias ($V_g = 0$ V) and **b)** at $V_g = -2$ V under continuous wave excitation (785 nm). Intensities were obtained from Lorentzian fits to the spectra in **Figure S15**. **c, d)** Ratios of the integrated PL intensities (E_{11}^*/E_{11} and E_{11}^{*-}/E_{11}) show that the emission of E_{11}^* and E_{11}^{*-} defect states saturates at higher excitation densities when a voltage ($V_g = -2$ V) is applied **(d)** compared to the neutral state **(c)**.

Estimation of Excitation Densities in EL and PL Spectroscopy of SWCNT Networks

To rationalize the differences in defect emission intensities relative to the E_{11} exciton, we estimate the excitation densities in the different experiments as outlined in the following.

In EL measurements, the excitation density is determined by the source-drain current within the transistor channel. A current of 100 μA corresponds to $\sim 6.2 \times 10^{14}$ charges per second, which is identical to the number of excitons per second assuming that every charge carrier recombines to form an exciton. The total channel width is 10 mm (interdigitated electrodes) and we assume a width of 2 μm for the recombination zone. To calculate the areal density of SWCNTs, we use an average length of $\sim 1.5 \mu\text{m}$ and a linear density of $\sim 20 \mu\text{m}^{-1}$ for the dense networks. Thus, the areal density is ~ 21 SWCNTs per μm^2 using the formula from Statz *et al.*¹ With an exciton lifetime of ~ 100 ps, we obtain an instantaneous excitation density of $\sim 1.5 \times 10^{-1}$ excitons per SWCNT. This calculation is identical to Naber *et al.* except that the quantum yield is not considered here, since we are interested in the overall excitation density rather than the exciton density available for lasing.²

In PL experiments with pulsed laser excitation, samples were excited with the output of a supercontinuum laser (20 MHz repetition rate, ~ 6 ps pulse width, 575 nm excitation wavelength). The average laser power in the excitation spot was $\sim 10 \mu\text{W}$, corresponding to $\sim 1.5 \times 10^6$ photons per pulse. With the photon energy, we can calculate the number of photons per time and per pulse. To estimate the number of absorbed photons, the peak absorption coefficient for excitation at the E_{22} transition as determined by Streit *et al.*³ and the geometrical factor of 88,000 carbon atoms per μm nanotube length for (6,5) SWCNTs are used. With an areal density of ~ 21 SWCNTs per μm^2 as detailed above, and a laser spot size of $\sim 2 \mu\text{m}$ in diameter, we calculate an excitation density of $\sim 3.4 \times 10^1$ excitons per SWCNT and pulse. This result is in good agreement with Ma *et al.* who estimated ~ 3 E_{11} excitons per 1 μW pump laser power for pulsed excitation at the E_{22} transition.⁴

Consequently, the exciton densities under pulsed optical excitation are significantly (~ 100 times) higher compared to electrical excitation. Due to state filling, sp^3 defect emission saturates at lower excitation powers than emission from the mobile E_{11} exciton.^{5,6} Hence, the difference in defect emission intensities (considerably higher defect emission in EL compared to PL under pulsed E_{22} excitation) is inferred to result from the different excitation density regimes.

For PL experiments under continuous wave excitation at 785 nm, the density of generated excitons cannot be estimated since the absorption cross section for this off-resonant excitation wavelength is unknown. However, from the laser power-dependent PL measurements (see **Figures S15 and S16**), it is evident that excitation powers for the acquisition of the spectra in **Figures 4 and S12** were in the linear regime and no state-filling is observed. This notion is further corroborated by the near-identical E_{11}^*/E_{11} peak ratios as shown in **Figure S11**, suggesting similar excitation density regimes in EL and non-resonant (785 nm cw excitation) PL experiments.

Charge Modulation Photoluminescence Spectroscopy

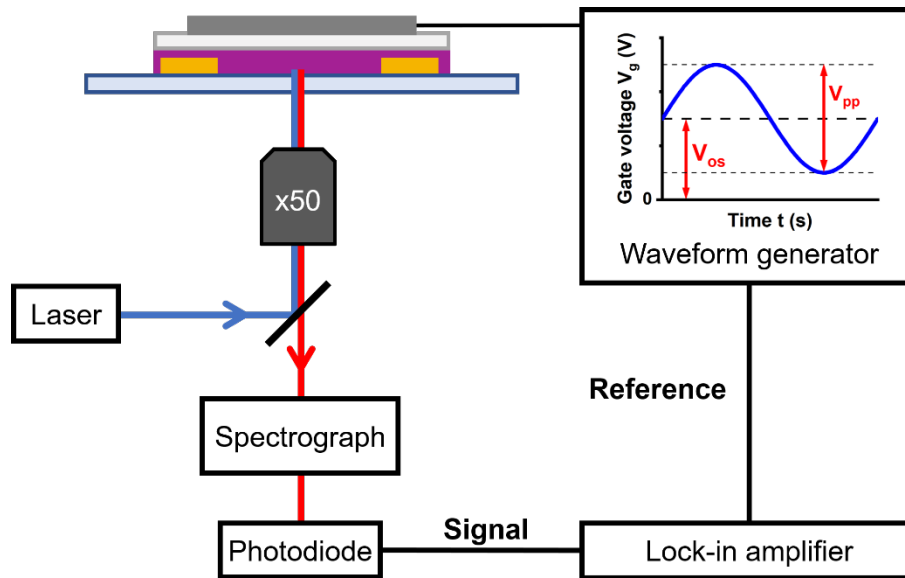


Figure S17. Schematic setup for charge modulation photoluminescence (CMPL) spectroscopy. SWCNT network FETs are optically excited with a 785 nm laser diode operated in continuous wave mode. The charge carrier density in the FET channel is modulated with a waveform generator by applying a sinusoidal bias (offset voltage, V_{os} ; peak-to-peak voltage, V_{pp}) to the gate electrode. The emission is spectrally resolved and the signal is detected with an InGaAs photodiode. A lock-in amplifier, which is fed with the sinusoidal bias from the waveform generator, recovers the differential change in PL (ΔPL) by phase-locking the photodiode signal to the reference signal.

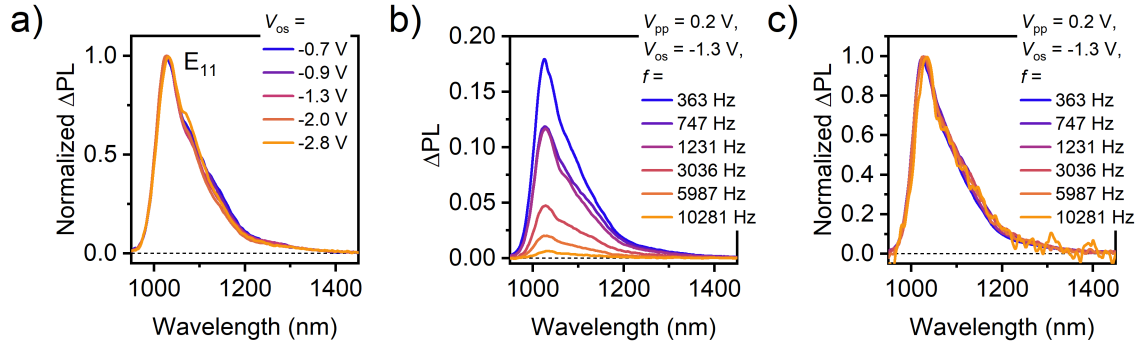


Figure S18. **a)** Normalized voltage-dependent CMPL spectra (absolute intensities shown in **Figure 5a** of the main text) of a pristine (6,5) SWCNT network (modulation frequency $f = 363$ Hz, peak-to-peak voltage $V_{pp} = 0.2$ V). **b)** Frequency-dependent CMPL spectra of a pristine SWCNT network and **c)** spectra normalized to the E_{11} ΔPL signal. The nearly identical normalized spectra confirm the common physical origin (*i.e.*, quenching by mobile charges) of the peaks.

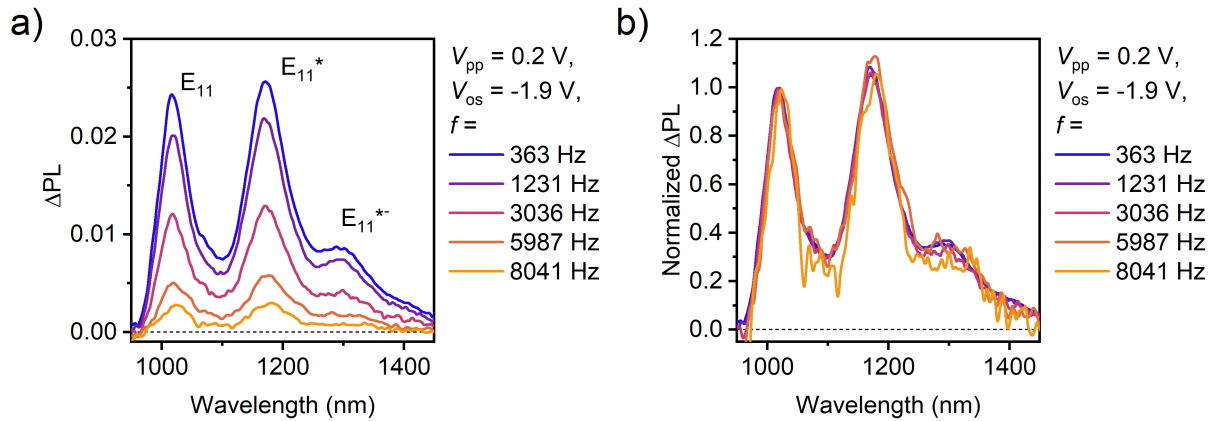


Figure S19. **a)** Frequency-dependent CMPL spectra of an sp^3 -functionalized SWCNT network with high defect density and **b)** spectra normalized to the E_{11} ΔPL signal. The nearly identical normalized spectra confirm the common physical origin (*i.e.*, quenching by mobile charges) of the peaks.

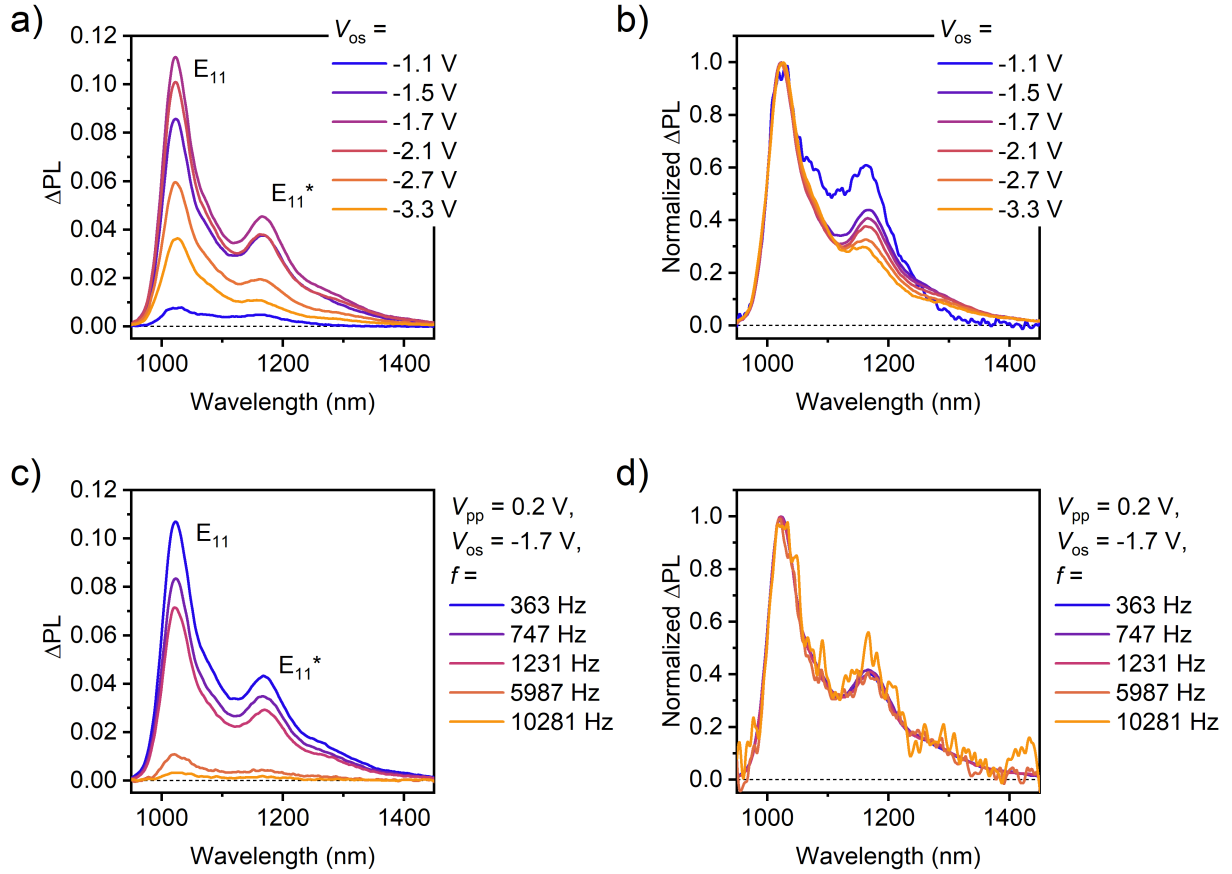


Figure S20. **a)** Voltage-dependent CMPL spectra of a sp^3 -functionalized SWCNT network with low defect density (modulation frequency $f = 363$ Hz, peak-to-peak voltage $V_{pp} = 0.2$ V) and **b)** spectra normalized to the E_{11} ΔPL signal. **c)** Frequency-dependent CMPL spectra of an sp^3 -functionalized SWCNT network with low defect density and **d)** spectra normalized to the E_{11} ΔPL signal. The nearly identical normalized spectra confirm the common physical origin (*i.e.*, quenching by mobile charges) of the peaks.

Temperature-Dependent Electrical Characterization of SWCNT FETs

Extraction of Trap Densities from the Subthreshold Regime

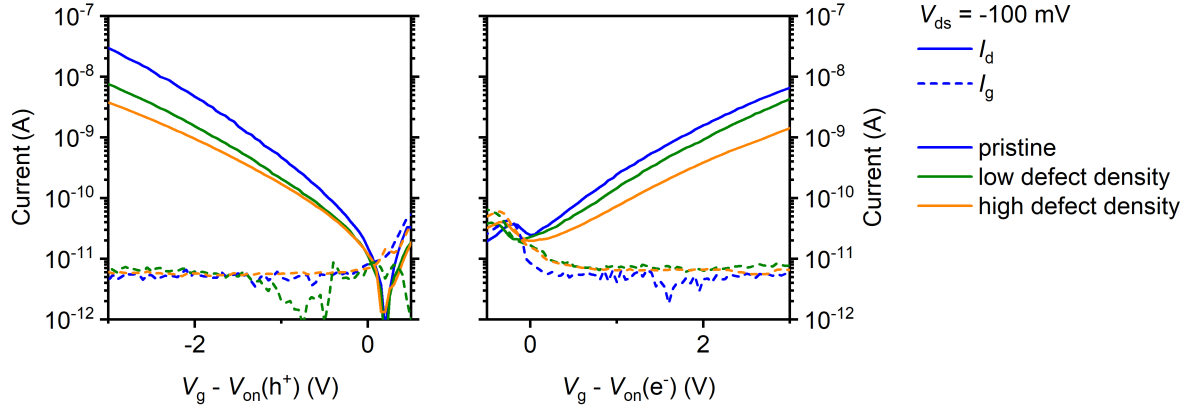


Figure S21. Zoom-in on the subthreshold regime in the transfer characteristics (source-drain voltage $V_{ds} = -100$ mV, $T = 300$ K) of pristine and sp^3 -functionalized SWCNT network FETs (drain currents, solid lines; gate leakage currents, dashed lines).

As detailed by Kalb *et al.* the relation between the subthreshold swing S and the trap density N_{\square} is given by the following formula.⁷

$$S = \frac{k_B T \ln(10)}{e} \left(1 + \frac{e^2}{C_i} N_{\square} \right) = \frac{\partial V_g}{\partial (\log(I_d))} \quad (1)$$

In Equation (1), k_B is the Boltzmann constant, T is the temperature, e is the elementary charge, and C_i is the areal capacitance. The calculated values for the trap densities are provided in **Table S2**.

Table S2. Trap density for holes and electrons calculated from the subthreshold slopes of the transfer characteristics of pristine and sp^3 -functionalized SWCNT network FETs shown in **Figure S21** according to Equation (1).

	Trap density for holes $N_{\square}(h^+) \text{ (cm}^{-2} \text{ eV}^{-1}\text{)}$	Trap density for electrons $N_{\square}(e^-) \text{ (cm}^{-2} \text{ eV}^{-1}\text{)}$
Pristine	$(5.9 \pm 0.3) \cdot 10^{12}$	$(10.1 \pm 0.1) \cdot 10^{12}$
Low defect density	$(8.3 \pm 0.3) \cdot 10^{12}$	$(13.1 \pm 0.1) \cdot 10^{12}$
High defect density	$(9.4 \pm 0.3) \cdot 10^{12}$	$(16.0 \pm 0.1) \cdot 10^{12}$

Schematic Device Layout and Principle of Gated Four-Point Probe Measurements

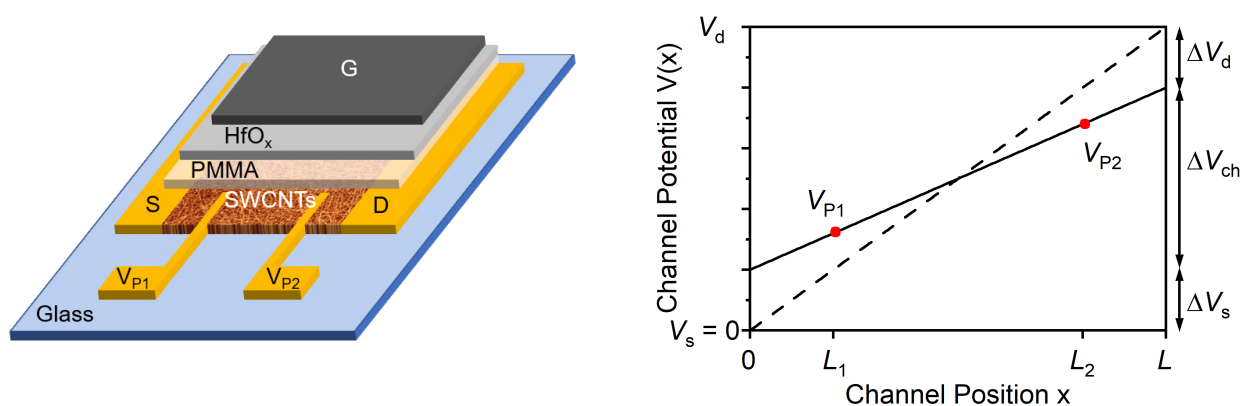


Figure S22. Working principle of gated four-point probe measurements. As shown in the schematic device layout (layers are laterally shifted and scaled for better visibility), two voltage probes (V_{P1} , V_{P2}) are defined at the positions $L_1 = 8 \mu\text{m}$, $L_2 = 32 \mu\text{m}$ within the channel ($L = 40 \mu\text{m}$). By linearly extrapolating the potential gradient in the transistor channel measured with the voltage probes (solid line), the potential drops at the source and drain electrodes (ΔV_s , ΔV_d) are determined and thus the contact resistance can be calculated. ΔV_{ch} is the actual channel potential, and the dashed line corresponds to an ideal case without any contact resistance.

Temperature-Dependent Mobilities

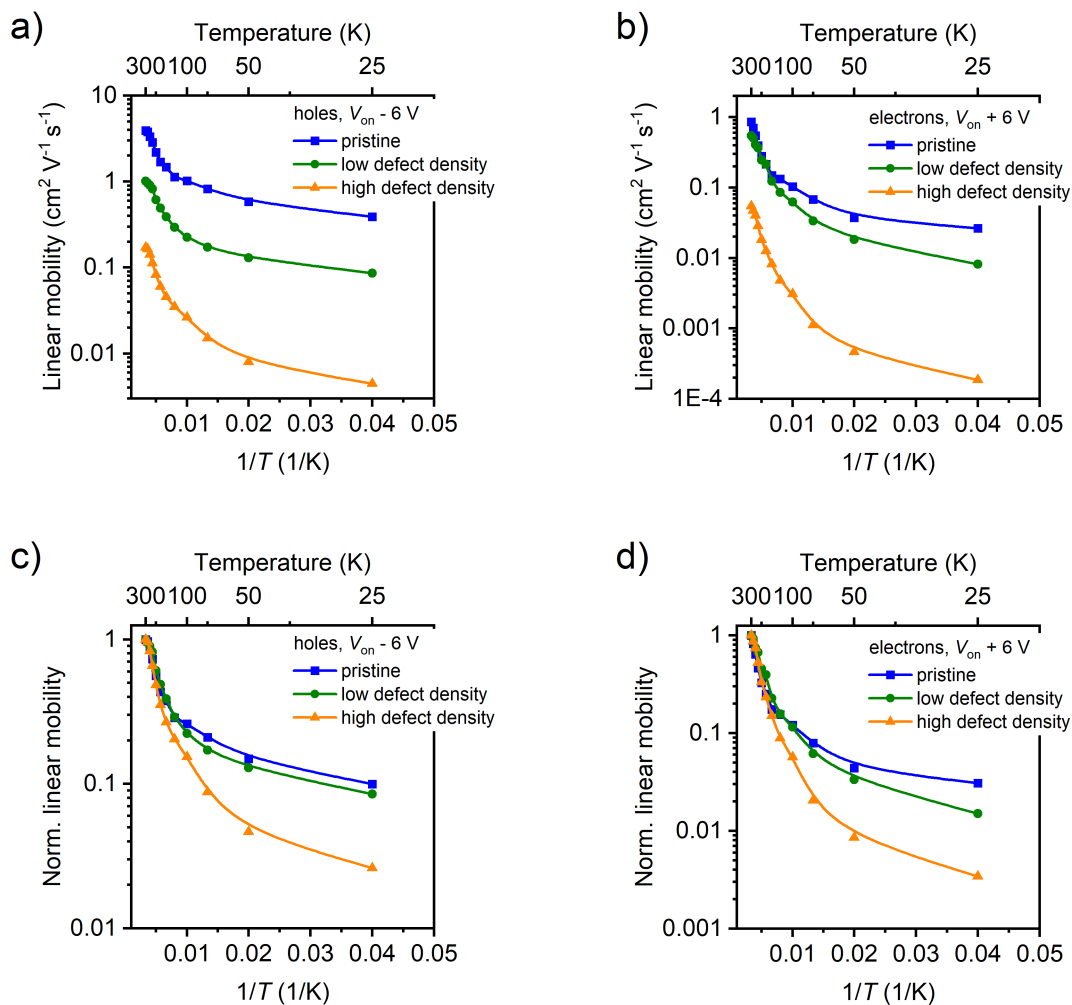


Figure S23. Full dataset of temperature-dependent, contact resistance-corrected linear mobilities of pristine and sp^3 -functionalized SWCNT network FETs. Graphs show **a, b)** absolute and **c, d)** normalized mobilities in the hole and electron transport regimes, respectively. For better comparison, all values were extracted at a fixed gate voltage overdrive of $\pm 6 \text{ V}$ for electrons and holes, respectively.

REFERENCES

1. Statz, M.; Schneider, S.; Berger, F. J.; Lai, L.; Wood, W. A.; Abdi-Jalebi, M.; Leingang, S.; Himmel, H.-J.; Zaumseil, J.; Siringhaus, H. Charge and Thermoelectric Transport in Polymer-Sorted Semiconducting Single-Walled Carbon Nanotube Networks. *ACS Nano* **2020**, *14*, 15552-15565.
2. Naber, R. C. G.; Bird, M.; Siringhaus, H. A Gate Dielectric That Enables High Ambipolar Mobilities in Polymer Light-Emitting Field-Effect Transistors. *Appl. Phys. Lett.* **2008**, *93*, 023301.
3. Streit, J. K.; Bachilo, S. M.; Ghosh, S.; Lin, C.-W.; Weisman, R. B. Directly Measured Optical Absorption Cross Sections for Structure-Selected Single-Walled Carbon Nanotubes. *Nano Lett.* **2014**, *14*, 1530-1536.
4. Ma, X.; Hartmann, N. F.; Velizhanin, K. A.; Baldwin, J. K. S.; Adamska, L.; Tretiak, S.; Doorn, S. K.; Htoon, H. Multi-Exciton Emission from Solitary Dopant States of Carbon Nanotubes. *Nanoscale* **2017**, *9*, 16143-16148.
5. Iwamura, M.; Akizuki, N.; Miyauchi, Y.; Mouri, S.; Shaver, J.; Gao, Z.; Cognet, L.; Lounis, B.; Matsuda, K. Nonlinear Photoluminescence Spectroscopy of Carbon Nanotubes with Localized Exciton States. *ACS Nano* **2014**, *8*, 11254-11260.
6. Berger, F. J.; Lüttgens, J.; Nowack, T.; Kutsch, T.; Lindenthal, S.; Kistner, L.; Müller, C. C.; Bongartz, L. M.; Lumsargis, V. A.; Zakharko, Y.; Zaumseil, J. Brightening of Long, Polymer-Wrapped Carbon Nanotubes by sp^3 Functionalization in Organic Solvents. *ACS Nano* **2019**, *13*, 9259-9269.
7. Kalb, W. L.; Batlogg, B. Calculating the Trap Density of States in Organic Field-Effect Transistors from Experiment: A Comparison of Different Methods. *Phys. Rev. B* **2010**, *81*, 035327.